Scalar dissipation rate statistics in turbulent swirling jets

V. Stetsyuk,[1, 2, a)] N. Soulopoulos,[2] Y. Hardalupas,[2] and A. M. K. P. Taylor[2]

[1)] *University of Huddersfield, Queensgate, Huddersfield, HD1 3DH,*
UK

[2)] *Imperial College London, London, SW7 2AZ, UK*

(Dated: 10 June 2016)

The scalar dissipation rate statistics were measured in an isothermal flow formed by discharging a central jet in an annular stream of swirling air flow. This is a typical geometry used in swirl-stabilised burners, where the central jet is the fuel. The flow Reynolds number was 29000, based on the area-averaged velocity of 8.46 m/s at the exit and the diameter of 50.8 mm . The scalar dissipation rate and its statistics were computed from two-dimensional imaging of the mixture fraction fields obtained with planar laser induced fluorescence of acetone. Three swirl numbers, S, of 0.3, 0.58 and 1.07 of the annular swirling stream were considered. The influence of the swirl number on scalar mixing, unconditional and conditional scalar dissipation rate statistics were quantified. A procedure, based on a Wiener filter approach was used to de-noise the raw mixture fraction images. The filtering errors on the scalar dissipation rate measurements were up to 15%, depending on downstream positions from the burner exit. The maximum of instantaneous scalar dissipation rate was found to be up to 35 s^{-1}, while the mean dissipation rate was 10 times smaller. The probability density functions of the logarithm of the scalar dissipation rate fluctuations were found to be slightly negatively skewed at low swirl numbers and almost symmetrical when the swirl number increased. The assumption of statistical independence between scalar and its dissipation rate was valid for higher swirl numbers at locations with low scalar fluctuations and less valid for low swirl numbers. The deviations from the assumption of statistical independence were quantified. The conditional mean of the scalar dissipation rate, the standard deviation of the scalar dissipation rate fluctuations, the weighted probability of occurrence of the mean conditional scalar dissipation rate and the conditional probability are reported.

[a)]Corresponding author:v.stetsyuk@hud.ac.uk

I. INTRODUCTION

The dissipation rate, which is identified as a characteristic diffusion time scale imposed by the mixing field[1], requires modelling in essentially all computational models for non-premixed combustion. The scalar dissipation rate can be used for instance in a PDF-flamelet approach in which species mass fraction, mean reaction rate, temperature etc. are pre-computed as a function of two variables, namely mixture fraction and the scalar dissipation rate and stored in a library. The scalar dissipation rate was also identified as the criterion that was able to predict the local extinction phenomenon of diffusion flames. It was pointed out that local extinction of diffusion flames occurred where the conditional dissipation rate exceeded a critical quenching value and global extinction took place when the cumulative probability of the conditional dissipation rate exceeded a critical threshold[1–4].

In the context of combustion modelling that is based on ensemble-averaged (RANS) or spatially-averaged (LES) equations describing the fluid motion, the probability distribution of the conditional scalar dissipation rate and the corresponding mean value must also be known. A common practice is based on the assumption of statistical independence between the scalar and its dissipation rate, which means that their joint probability density function is equal to the product of their individual probability density functions[4,5]. The probability density function of the conditional scalar dissipation rate was typically assumed to be log-normally distributed, as it was firstly suggested by Kolmogorov[6]. A detailed knowledge of the statistical properties of mixture fraction fluctuations and their conditional dissipation rate is also required in conventional flamelet methods, advanced flamelet and transported PDF methods, which include the fluctuations of the scalar dissipation rate[7–9], stochastic well-stirred reactor models[10] and conditional moment closure models[11]. Measurements of scalar dissipation rate and its statistics (conditional and unconditional) are rare despite their importance for a wide range of turbulent flow applications, especially in complex flows.

Assumptions of, e.g. statistical independence in simple jet flows may not be valid in complex (swirling) flows. Moreover, flows with high and low swirl numbers may exhibit different behaviour in terms of statistics of scalar dissipation rate and mixture fraction. In addition, transition from low to high swirl number, and wise versa, can qualitatively change assumptions that are adopted in computational fluid dynamics. Indeed, it will be demonstrated later that statistical dependence is valid for flows with high swirl number. In

this context, the swirl number is the key variable that influences the flow behaviour and hence, all the statistics should be linked to this single parameter.

In the context of combustion calculations three parameters are usually required; the mean scalar dissipation rate conditional on the stoichiometric mixture fraction, the weighted probability of occurrence of the mean conditional scalar dissipation rate and the standard deviation of conditional dissipation rate. The weighted probability of occurrence of the mean conditional scalar dissipation rate represents the molecular diffusion in scalar space in the transport equation for the scalar p.d.f. and is proportional to the mean reaction rate[12]. The conditional scalar dissipation rate is also proportional to the mean reaction rate[13]. Mastorakos[14] demonstrated that the probability of autoignition was proportional to conditional scalar dissipation rate. The maximum of conditional scalar dissipation rate was not the stoichiometric mixture fraction as it would have been intuitively expected. In addition, the extinction of a diffusion flame occurs when the conditional scalar dissipation rate exceeds a certain value[14].

The conditional mean, the weighted probability of occurrence and the standard deviation of fluctuations of conditional dissipation rate are computed as follows:

$$\langle \chi | z_{st} = z^* \rangle \equiv \int_0^\infty \chi P\left(\chi | z_{st}\right) d\chi = \frac{1}{N_{st}} \sum_{i=1}^{N_{st}} \left(\chi | z_{st}\right) \tag{1}$$

$$E_{\chi|z} \equiv \langle \chi | z_{st} = z^* \rangle P\left(z = z_{st}\right) \tag{2}$$

$$\begin{aligned} \langle \chi^{'} | z_{st} = z^* \rangle &\equiv \left(\int_0^\infty \left(\chi - \langle \chi | z_{st} \rangle \right)^2 P\left(\chi | z_{st}\right) d\chi \right)^{1/2} = \\ &= \left(\frac{1}{N_{st}} \sum_{i=1}^{N_{st}} \left(\chi | z_{st} - \langle \chi | z_{st} \rangle \right)_i^2 \right)^{1/2} \end{aligned} \tag{3}$$

where χ is scalar dissipation rate, z_{st} is stoichiometric mixture fraction, P is probability density function, $\langle \chi | z_{st} = z^* \rangle$ is mean scalar dissipation rate conditional on the stoichiometric mixture fraction, $E_{\chi|z}$ is weighted probability of occurrence of the mean conditional scalar dissipation rate, $\langle \chi^{'} | z_{st} = z^* \rangle$ is standard deviation of conditional dissipation rate, N_{st} is number of scalar dissipation rate samples corresponding to the stoichiometric mixture fraction. The averaging denoted by the angular brackets is only carried out for events that satisfy the conditions to the right of the vertical rule.

3

Measurements of the scalar dissipation rate are not straightforward due to temporal and spatial resolution requirements. Such measurements require high spatial resolution, which is comparable to Batchelor or Kolmogorov length scale (for Schmidt number equal to one). These requirements are not easily achieved in practice due to optical system limitations, e.g. laser sheet thickness, optical aberrations etc. Effective resolution and noise-induced apparent dissipation, i.e. artificial over- or underestimation of scalar dissipation rate are mainly determined by the system transfer function[15],[16]. The system transfer function will be dependent on optics quality, experimental system alignment and random fluctuations of noise in the measured data and is discussed later in the manuscript. Appropriate de-noising techniques must be used in order to obtain meaningful statistics of scalar dissipation rate. A description of de-noising technique, which is employed in this work to obtain 'true' scalar dissipation rates, will be discussed in subsequent sections.

Measurements of scalar dissipation rate have been demonstrated in a number of papers. Dibble[17] presented the first laser-based measurements of scalar dissipation rate in turbulent non-premixed, non-reacting jets and the first laser-based or otherwise in reacting jet flames by using an optical multichannel analyser. Scalar dissipation rate measurements and associated issues were also reported in a number of papers[18–28]. Even though the scalar dissipation rate and structural information about the scalar fields was addressed in a number of papers, the statistics were limited to either counterflow geometry or to non-swirling jets. The scalar dissipation rate statistics in turbulent swirling flows have not been examined to the best of our knowledge. Our aim is, therefore, to extend knowledge to configurations relevant to practical combustors, which are typically based on swirl-stabilized burners. In this context, the primary goal of the present work was to provide the statistical information, relationships between scalar fluctuations and their dissipation rate, as well as to present both unconditional and conditional scalar dissipation rate statistics.

Though the computation of scalar dissipation rate generally involves the computation of 3D gradient of the mixture fraction, it is practically hard to measure the 3D fields of mixture fraction. In homogeneous and isotropic turbulent fields, the three-dimensional scalar dissipation rate can be easily calculated, because the statistics of the mixture fraction fluctuations are the same in all three directions. In this case, one of the components can be measured and the calculation of the scalar dissipation rate is quite straightforward. The scalar dissipation rate, like other variables in turbulent flows, fluctuates in time and space

and its formal definition is given by the following formula, where the diffusivity for the scalar (acetone vapour), D_a, is assumed to be constant and equals to 0.124 cm^2/s.

$$\chi_z = 2D_a \left[\left(\frac{\partial z}{\partial x} \right)^2 + \left(\frac{\partial z}{\partial y} \right)^2 \right] \tag{4}$$

where z is mixture fraction, D_a is acetone diffusivity in air and x and y are spatial coordinates correspondingly

The remaining paper is structured as follows: The next section describes the swirling air flow burner and the optical instrumentation used to measure the scalar (mixture fraction), which was then used to evaluate the mixture fraction scalar dissipation rate. The spatial requirements and de-noising technique for the dissipation rate measurements are also briefly discussed. The last section describes the results and discusses the findings. The paper ends with a summary of the main conclusions.

II. EXPERIMENTAL ARRANGEMENT AND INSTRUMENTATION

A. Experimental setup

The flow section (item 15 in Fig. 1) consisted of two concentric pipes with the annulus supplying swirling air and the central pipe delivering air seeded with acetone vapour (measured scalar quantity)[29,30]. The central pipe (fuel) had an inner diameter D_f of 15 mm and an outer diameter of 18 mm, was 0.75 m long and was located concentrically in the outer pipe of inner diameter, D of 50.8 mm and centred within it by three screws at 25 mm upstream of the burner exit. The flow development section was 0.264 m long.

The annular air stream was split into two separately metered streams named 'swirling' and 'axial' air (Fig. 1). The swirling stream was created by passing air through a static swirler containing six milled tangential slots to impart angular momentum. The static swirler was located in a plenum chamber in which the swirling air was combined with the second stream that delivered 'axial air'. Metal plates were installed in the axial and tangential air sections of the plenum chamber to ensure that the axial and tangential air streams were distributed uniformly upstream of the inlets into the annular air supply stream of the burner, where they were combined to control the strength of swirl at the burner exit. The tangential and axial air flowrates were metered by flowmeters after correction to atmospheric pressure and

5

temperature. The axial direction, parallel to the flow propagation, was denoted as 'y' and the radial direction, perpendicular to the main direction of the flow, as 'x'. The swirl number used as the primary variable was computed by using the velocity profiles obtained by Laser Doppler Anemometry[30]. The swirl number is defined as follows:

$$S = \frac{2G_\Theta}{G_Z D} \tag{5}$$

$$G_\Theta = 2\pi\rho \int\limits_{r=r_i}^{R} WrUrdr$$
$$G_Z = 2\pi\rho \int\limits_{r=r_i}^{R} UUrdr \tag{6}$$

where r_i is radius of the inner pipe, ρ is density, U is axial velocity component, W is tangential velocity component, G_Θ is axial flux of angular momentum, G_z is axial flux of axial momentum, S is swirl number, R is radius of the outer pipe, D is diameter of the outer pipe.

All swirling flows can generally be split into two groups i.e. weak ($S < 0.6$) and strong ($S > 0.6$) swirling flows. From the survey of experimental studies of swirling flows a qualitative picture can be drawn. For low swirl numbers $S < 0.5$, the flow patterns demonstrate so-called a 'solid body' rotation, which is initially observed at $S \approx 0.1$. For high swirl number $S > 0.5$, flow develops a structure with rapidly rotating core, which is surrounded by annulus of low vorticity. A flow reversal is observed in the central region of the swirling flow[31]. Even though, weak swirling flows have limited industrial applicability it is necessary to investigate such regimes and compare with highly swirled flows, especially when statistics of the scalar dissipation is considered. In this work, swirl numbers $S = \{0.3, 0.58, 1.07\}$ were chosen to be the same as it was chosen by Milosavljevic[30] for consistency and completeness. In addition, the same burner will be used to study reacting swirling flows, flame stabilisation and thermal dissipation rates. The flame stabilisation is affected by the swirl number and, therefore, both low and high swirl numbers have to be considered.

The Reynolds numbers in the central (fuel) pipe and in the 'secondary air' coflow stream were 3770 and 28662 respectively based on the bulk velocity of 3.77 m/s, 8.46 m/s and the pipe diameter of $D_f = 15$ mm, $D = 50.8$ mm. The Batchelor length scale was in the range of $\approx$300-400 μm for the range of S of 0.3-1.07 and was computed from the dissipation rate spectra at the wavenumber corresponding to 2% of the peak value of the dissipation rate

spectrum. The dissipation rate spectra were computed as the average of the squared Fourier transform of the fluctuations of the axial and radial gradients of the mixture fraction. The mean mixture fraction gradient in the axial direction was subtracted from instantaneous values of the gradient of the mixture fraction in the axial direction. The final dissipation rate spectra, computed from 1500 images, were finally spatially averaged so as to obtain the averaged spectra in the axial or radial directions. Examples of the spectra for the central jet flow and the flow with S=0.3 are shown in Figure 2. An extended inertial range is seen for the flow with S=0.3, thus suggesting that Batchelor scale should be less than in case of central jet flow (non-swirling flow). It is also interesting to note that the Batchelor scale obtained from the spectrum that was computed from radial-derivative is smaller than that from the spectrum computed from axial-derivative. This suggests that turbulence is more developed and intensive in radial direction, which is also expected in swirling flows.

A Q-switched Nd:YAG frequency-quadrupled 266 nm laser from Continuum Inc. (item 3 in Fig. 1) was used to excite the acetone vapour fluorescence. The laser pulse width was in the range of 5-7 ns at Full Width at Half Maximum (FWHM). A single dichroic mirror (item 2 in Fig. 1) was used to decrease the amount of 532 nm light reaching the burner and to steer the laser beam from the laser exit port towards the experimental setup and sheet forming optics. The sheet forming optics consisted of a single cylindrical positive lens with a focal length of 310 mm (item 1 in Fig. 1). The lens was used to focus the laser beam into a thin waist, with focal point located at the axis of symmetry of the flow. The average laser energy delivered at the test section was 75 mJ/pulse.

An Imager Intense® CCD camera from LaVision Inc. was used to record the images (item 12 in Fig. 1). This camera was equipped with a 50 mm f1.4 Nikkor lens. A 13 mm extension ring was also used after the camera lens for closer focusing. A BG3 bandpass Schott filter (item 13 in Fig. 1) was used in front of the camera lens in order to block any remaining 532 nm light that might interfere with the acquired signal. The optical magnification was determined by using a calibration target plate and was found to be 0.0263 mm/pixel.

The laser beam waist was measured directly by using a CCD camera technique. The positive cylindrical lens was rotated to $90\,°$, so the laser sheet thickness could be captured by measuring the intensity of acetone vapour fluorescence. Averaging of 50 images minimized laser beam intensity fluctuations. The beam waist was defined as the diameter where the beam irradiance was $1/e^2$ or 0.135 times its maximum value and found to be 0.158 mm. The
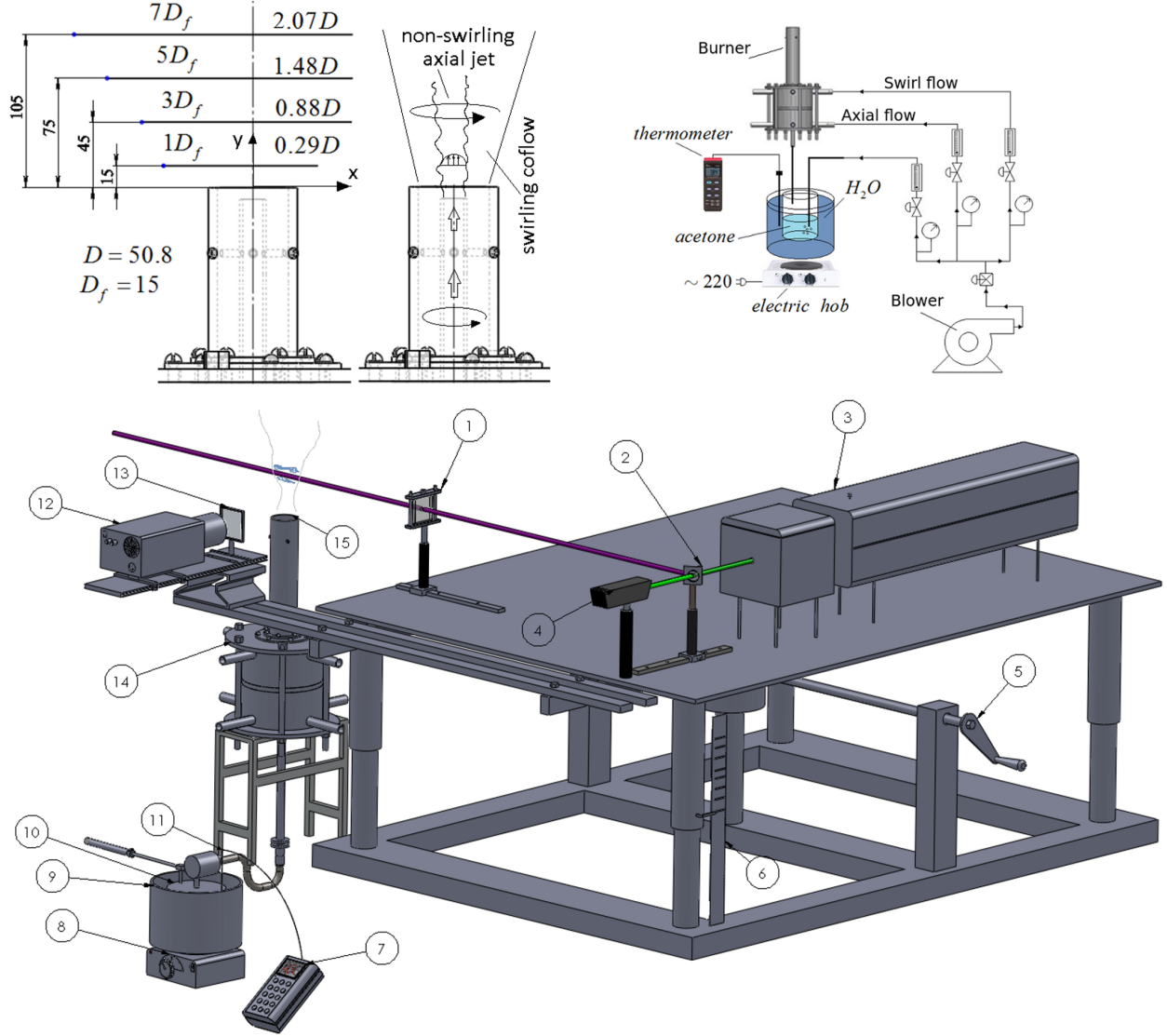
FIG. 1. A schematic view of laser sheet downstream positions during measurements, flow arrangement (top) and the experimental setup (bottom). Laser sheet positions are shown in absolute values mm, normalized by the fuel pipe internal diameter $D_f = 15$ mm and by the burner internal diameter $D = 50.8$ mm. 1 - positive cylindrical lens (f=310 mm), 2 - dichroic mirror, 3 - laser, 4- beam dump, 5 - traverse handle, 6 - vertical ruler, 7 - thermometer, 8 - heater, 9 - acetone seeder, 10 - acetone container, 11 - thermocouple, 12 - CCD camera, 13- BG3 bandpass Schott filter.

average laser sheet intensity distribution used in the correction procedure was obtained by supplying acetone vapour through the axial fuel nozzle without air coflow and subsequent measuring the intensity at the jet potential core. In order to eliminate the dark noise, a set of images was recorded, averaged and then simply subtracted from each image obtained

during the experiments. No background image was recorded during experiments, because incident background light was blocked by the BG3 filter.

The synchronization of the laser flashlamp, the laser Q-switch and the camera was ensured by using a programmable PC-based timing unit (PTU) using TTL pulses. The laser flashlamp was fired continuously at 10 Hz. The laser Q-switch was triggered every time when an image was recorded. The camera was triggered at the same time as the Q-switch trigger (TTL pulse was sent to Q-switch and to the camera simultaneously) and camera exposure time was set to 1 μs. The camera shutter opened before the start of the laser pulse and closed after the end of the laser pulse. Both the laser and the camera were electronically controlled from software package DaVis 7.2©, provided by LaVision Inc., installed on a computer running Windows XP©.

A planar laser-induced fluorescence (PLIF) technique was used to obtain the acetone concentration fields (mixture fraction fields) in the isothermal swirling flow. The PLIF is a non-invasive measurement technique that can provide qualitative as well as quantitative characterization of the flow fields. The fluorescence signal is directly related to the concentration of tracer species in the flow being investigated and the laser energy. This technique can provide a set of detailed flow field maps both resolved spatially and temporally. The PLIF technique is, therefore, an ideal method to study non-reacting flows in various combustion systems. Moreover, PLIF technique can be used under a wide range of operating conditions and, therefore, has been widely applied to study various aspects of mixing in non-reacting jets.

Acetone has been used as a tracer for many years. The choice of acetone is simple due to its outstanding properties and in many ways can be regarded as an ideal tracer for the PLIF technique due to its linear relationship between the fluorescent intensity, laser power and acetone concentration in the flow. Acetone has also an accessible absorption spectrum at the UV. The fluorescent signal is emitted in the visual range of light spectrum 350-600 nm and the corresponding peak of the fluorescent emission spectrum is between 450 to 500 nm. Fluorescent signal can be recorder onto a digital sensor of a CCD camera and after which can be post processed as required. Moreover, the signal from acetone fluorescence is relatively high and its interpretation in actual fuel concentration is in fact straightforward.

The PLIF method is based on molecule excitation to a higher electronic energy level by absorbing the energy of a laser beam. The molecule at this energy state is unstable and will

go from upper energy level to the lower energy level emitting photon of the same energy as the original absorbed photon. The emitted photon can be detected and used to measure the light intensity, which is proportional to a number of molecules, or simply concentration of a tracer. The measured acetone fluorescent signal (the total number of photons) at each pixel position on the CMOS sensor (x, y) can be written as follows:

$$S_F(x, y) = \eta_{ef} \frac{\Omega}{4\pi} f_1(T) \chi_m n V_c B_{12} E_v \frac{A_{21}}{A_{21} + Q_{21}} \qquad (7)$$

where η_{ef} is transmission efficiency of collection optics, Ω is solid angle collected by imaging optics, $f_1(T)$ is fractional population of lower laser-coupled state in the absence of the laser field, χ_m is the mole fraction of the absorbing species, n is the total gas number density, V_c is collection volume imaged onto photodetector element, B_{12} is Einstein B coefficient for single-photon laser stimulated process, Q_{21} is the collision transfer coefficient, E_v is the spectral fluence of the laser, A_{21} is Einstein A coefficient for spontaneous emission.

All the quantities in the equation above are dependent on the position in the flow via pressure, temperature and tracer's concentration. For conditions of constant temperature and pressure the ratio of acetone fluorescent signal over the fluorescent signal at a reference position of known acetone concentration can provide measurements of the mixture fraction. If the reference position is at the exit of the fuel nozzle in a potential core, where no mixing with ambient air occurs, then the above mentioned ratio is directly related to the mixture fraction $z(x, y)$.

$$z(x, y) = \frac{S_F(x, y)}{S_{F_{ref}}(x, y)} \qquad (8)$$

where $S_F(x, y)$ is measured acetone fluorescence intensity, $S_{R_{ref}}(x, y)$ is reference acetone fluorescence intensity.

The raw images that were recorded during PLIF experiments $I_{raw}(x, y)$ were corrected by using the following formula. This formula takes into account several different sources of noise.

$$I_{cor}(x, y) = \frac{I_{raw}(x, y) - I_{bgr}(x, y) - I_{dark}(x, y)}{L_{sh}(x, y)} \qquad (9)$$

where I_{cor} is corrected image of acetone fluorescence intensity, $I_{bgr}(x, y)$ is background image, I_{dark} dark image, i.e. image formed by a photodetector in absence of light, L_{sh} is average

laser sheet intensity distribution.

The background image $I_{bgr}(x, y)$ is usually acquired with the same camera settings and with the laser firing but without flow in the test volume. The background image that was acquired during experiments was blank, i.e. no photons were detected. This was achieved through BG3 filter that blocked ambient light. In addition, no reflections from the burner were observed. Reflections from the dust particles (due to 532 nm light wavelength component in the laser beam) that were present in the test volume were also blocked by the BG3 filter. The dark image was acquired with a cap placed on the lens and then was simultaneously subtracted from recorded images during imaging. The average laser sheet intensity distribution was obtained by supplying acetone vapour through the axial fuel nozzle without air co-flow and subsequent measuring the intensity in the jet potential core. The laser sheet profile measured in this way is negligibly different from the laser sheet profile that can be obtained from the dye cells[24]. The variations of the profile from laser shot-to-shot were negligible.

The reference position (fluorescence intensity) was at the exit of the fuel jet in a potential core, where no mixing with ambient air occurs (without swirling co-flow). In order to reduce uncertainties in acetone fluorescent intensity at a reference position of known acetone concentration, the reference measurements were obtained over a small square region (1×1 mm) within the potential core of the acetone vapour jet without co-flow of air and for air flow rate of 40 l/min passing through the acetone seeder. The acetone seeder (item 9 in Fig. 1) was placed on an electrical heater (item 8 in Fig. 1), which maintained constant temperature of $45°C$ in order to stabilise acetone evaporation rate. RS-1313 1-channel thermometer and an N-type thermocouple of 1.5 mm diameter and 500 mm length were used to measure acetone temperature in the acetone seeder. Post-processing of the raw images was performed by software developed in MATLAB©.

A set of reference measurements consisted of 2650 images was taken continuously in potential core at air flow rate of 40 l/min passing through the seeder. The relationship between the reference intensity and a number of acquired images was deduced. A six-degree polynomial fit was then used to approximate this relationship. This approximation was used in computation of reference intensity as a function of acquired images in order to reduce uncertainties in the fluorescent intensity at the reference position. The time-dependent fluorescent signal at a reference position is then given by the following equation as follows:

$$S_{Fref} = p1 \cdot N_{i,img}^5 + p2 \cdot N_{i,img}^4 + p3 \cdot N_{i,img}^3 + p4 \cdot N_{i,img}^2 + p5 \cdot N_{i,img} + p6 \qquad (10)$$

where N is the number of acquired images.

$$
\begin{aligned}
p1 &= -2.9668e - 014 \\
p2 &= 2.2016e - 010 \\
p3 &= -5.818e - 007 \\
p4 &= 0.00061902 \\
p5 &= -0.36668 \\
p6 &= 1105.4
\end{aligned}
\qquad (11)
$$

The fluctuations of the acquired acetone intensity are mainly due to the fluctuations in laser power from pulse to pulse. The fluctuations in laser power from pulse to pulse were minimised by using longer warm-up time (typically longer than 30 min) and were measured to be less than 3%, which is less than filtering errors of 15% (due to Wiener filtering procedure). It is, therefore, assumed that fluctuations in laser power from pulse to pulse should not significantly affect the absolute values of scalar dissipation rate.

B. Data processing

The most commonly used cameras in imaging experiments are currently based on CCD image sensors and the image quality is the most important characteristic. The image quality is related to the actual spatial resolution and the ability to record the contrast of a real object to the camera detector. The magnification (scale factor) of any optical system is typically determined by using a calibrating target with known spatial resolution, e.g. 1951 USAF resolution test chart. However, in several applications, the nominal spatial resolution (or magnification) is not a limiting factor and differs from the so-called 'real' spatial resolution. For instance, in mixture fraction gradient measurements (or scalar dissipation rate measurements) the point spread function (PSF), which is defined as the intensity distribution at an image plane, produced by imaging an infinitesimally small portion of light can represent the actual optical resolution[16].

The PSF is related to an optical transfer function (OTF) via a modulation transfer function (MTF). The OTF is defined as the ability to transfer the contrast of a real object
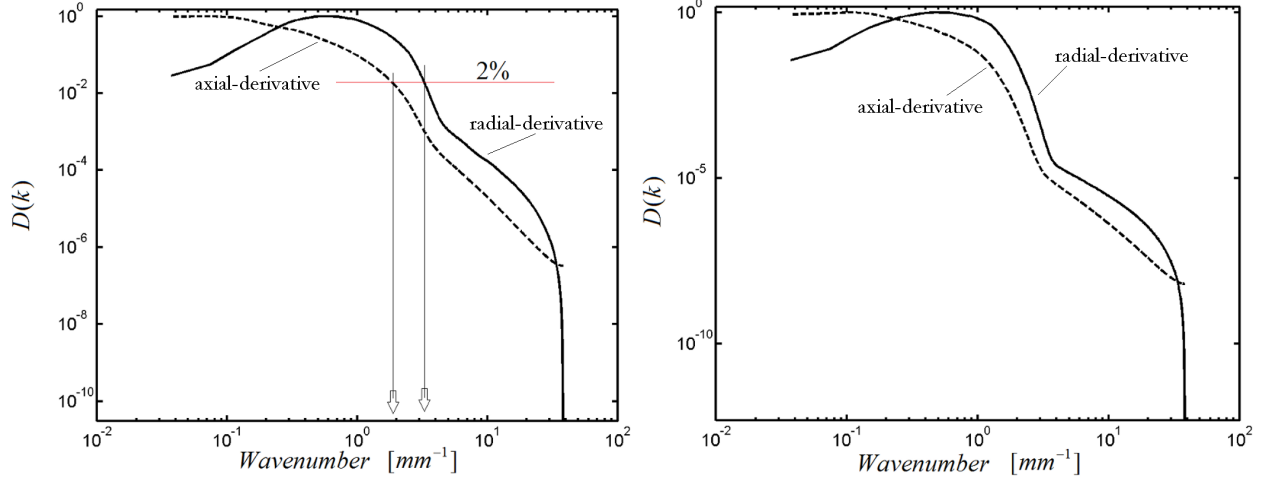
FIG. 2. Determination of the Batchelor length scale from the measured normalized dissipation rate power spectra at $y/D_f = 1$ for acetone vapour jet only without coflow (left) and S=0.3 (right). Vertical lines denote the position of the wavenumber corresponding to 2% of the spectrum peak value. The dissipation rate spectrum was normalized by its maximum. Solid line - denotes the dissipation rate spectrum computed from radial-derivative; dashed line $--$ denotes the dissipation rate spectrum computed from axial-derivative.

to the image plane at various spatial frequencies. The modulation transfer function, which is the Fourier transform of the PSF can be measured by various methods, e.g. knife-edge scanning technique and a slant edge method. In this work, we used the slant edge method due to its simplicity and fast measuring time. The detailed description of this method can be found in ISO 12233:2000 (Photography. Electronic still-picture cameras. Resolution measurements) and is not presented here. The spatial resolution that corresponded to 50% MTF was computed to be $\approx$350 μm. In this study, the effective spatial resolution that was determined by the MTF and a proposed image denoising technique were appropriate for quantifying the 'true' scalar dissipation rate measurements[32].

In this work, the Wiener-Kolmogorov filtering procedure (Wiener filter for simplicity) was used to reduce noise that was present in the measured data. This filtering procedure is based on a signal comparison between noiseless (estimated) and noise corrupted signal (measured)[24,32,33]. In order to be able to compute the Wiener filter, the power spectral densities of both the noise-free image and the noise must be known, which are typically not known in advance. It was suggested[33,34] that a recorded set of images (measured mixture

13

fraction) can be used to estimate the general trend of the true signal spectral density and the corresponding variations of the noise density. If the general trend of the true signal is known, then it will be possible to model the true signal for the wave numbers, where the noise contributes significantly. A detailed description of the Wiener filter with application to scalar dissipation rate measurements is given by Soulopoulos[24,32]. In this research, the estimated scalar dissipation rates after filtering were accurate to within 15% depending on the swirl number and the axial positions in the flow[32].

The mixture fraction measurements are based on the linear scaling of the fluorescent intensity and; hence, the camera linearity is an important parameter. The camera linearity is the relationship between the intensity of the incoming light and CCD chip voltage (or camera signal). In this work, the camera linearity was measured by plotting the camera signal from each individual pixel as a function of exposure time. The relationship between the exposure time and the camera signal from all pixels was linear.

The unconditional statistics, which are useful for turbulent reacting flow models as, for example, advanced flamelet and transported p.d.f. closures, which include the fluctuations of the scalar dissipation rate, are presented here in terms of the probability density functions of the scalar dissipation rate at the various positions in the flow, for all axial locations and swirl numbers. Data for each p.d.f. was compiled by considering a local window of axial length of 1.58 mm $\approx 4\lambda_\beta$ and radial length of 3.87 mm $\approx 10\lambda_\beta$ containing 8820 data points and over 1500 images resulting in 13e9 dissipation rate data points for each spatial location. Window dimensions were chosen on the basis of sufficient number of samples and their locations were chosen to represent both homogeneous and highly segregated scalar fields, i.e shear layer and centreline. Five spatial locations were considered and are shown in Figure 3. All probability density functions of the scalar dissipation rate of the mixture fraction are presented here in terms of $P(C)$, where P denotes probability density function and C is defined as follows:

$$C = \frac{\ln{(\chi)} - \overline{\ln{(\chi)}}}{\sigma_{\ln(\chi)}} \qquad (12)$$

where $\sigma_{\ln(\chi)}$ is standard deviation of natural logarithm of scalar dissipation rate

In order to assess the effect of the chosen window size for calculation of the p.d.f., different window sizes were also tested. The p.d.fs. of the scalar dissipation rate were computed from window sizes ranging from 0.1×0.1 mm to 10×10 mm. The p.d.f. reproduced from

the smallest windows contained 24000 data points, while the p.d.f. reproduced from the larger windows consisted more than 13e6 values. The p.d.f. reproduced from the smallest regions reproduced the p.d.f. computed from the larger sample windows and its trend was well captured at high swirl numbers, i.e. 0.58-1.07 and all spatial window locations. For low swirl number of 0.3, deviations from p.d.fs. computed from large windows were sometimes observable. Nevertheless, the range of the dissipation fluctuations was well captured even if the p.d.f. was not fully converged. It can be suggested that in regions where high intermittency is observed the smallest window cannot provide an adequate description of the corresponding probability density function due to insufficient statistics. It was also noted that high intermittency was observed in low swirling flow with S=0.3.

It should be noted that the orientation of the scalar dissipation rate vector may be away from the plane of the measurements. The measurements presented here are the projection of the vector on the measurement plane. Depending on the swirl number, the orientation of the scalar dissipation rate vector can approach the measurement plane, e.g. for S=0.3. For higher swirl number, the orientation of the vector cannot be evaluated from planar measurements. However, if scalar dissipation rate is linked to the local mixing regime rather than to specific regions in the flow, it can be assumed that the conclusions from planar measurements are plausible. Direct extrapolation of presented results to reacting flows should also be considered carefully. It is practically hard to measure spatial distribution of mixture fraction in reacting flows. Therefore, simplified measurements are needed, which can be carefully extended to reacting flows. For instance mixing of reactants in swirling flows and subsequent ignition of 'distributed mixture fraction' in a flow recirculation zone. Prior to the flow recirculation zone there is pure mixing before flame stabilisation, where conclusions from this work may be considered.

C. Uncertainty in flow rate measurements

During experiments the air referred as to swirling component was measured by KDG Rotameter Series 2000 variable-area flowmeter, which was individually calibrated to accuracy of Class 1.6 i.e. $\pm 1.2\%$ of indicated flow and plus $\pm 10.4\%$ full scale reading. The axial component of air was measured by Fisher Control Limited flowmeter rated at a maximum flow of 1000 l/min. The flow rate of the mixture of acetone and air was measured by a
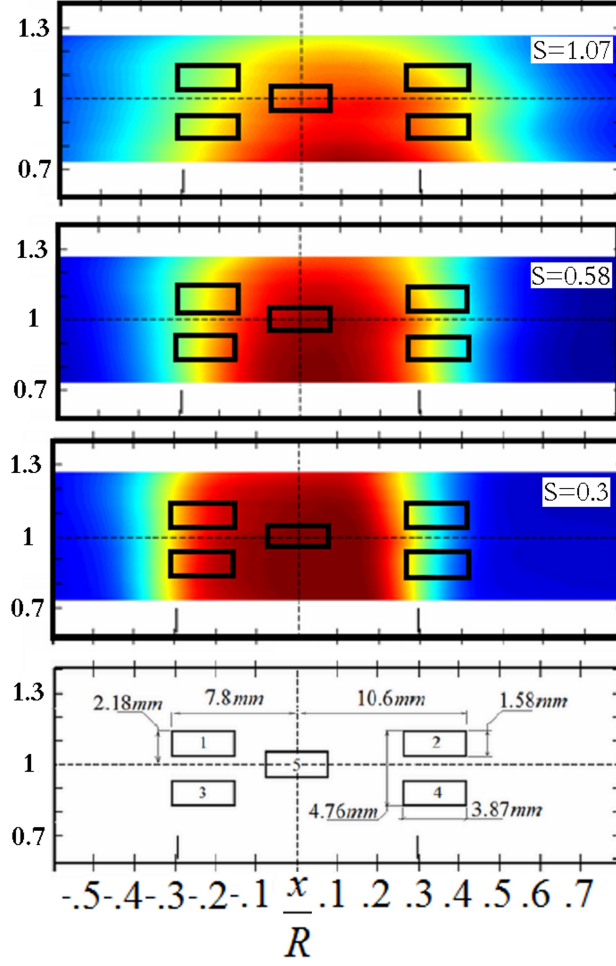
FIG. 3. Window positions, where scalar dissipation rate statistics were evaluated. Window positions 1,3 and 2,4 are located at different distance from the burner centreline. Window 5 is located at a cusp of the laser beam and at the burner centreline. The window positions are also shown with respect to spatially distributed mean mixture fraction for different swirl number and $y/D_f = 1$.

flowmeter from Platon Inc. (NGXV series) with the accuracy of $\pm 1.25\%$. The fluorescence intensity variation due to temperature variations was insignificant, based on $0.36\%/K$ decay for 266 nm[35].

The temperature in a stirred, isothermal bath of hot water was measured by the same equipment, which was used in air temperature measurements in the measurement plane. Uncertainty of the swirl numbers was computed as 0.3 ± 0.0152, 0.58 ± 0.0288 and 1.07 ± 0.0657. Uncertainty in Reynolds number was computed as 28662 ± 1456 (S=0.3), ±1422 (S=0.58) and ±1760 (S=1.07). Finally, uncertainty in bulk velocity of swirling co-flow was computed

16

as 8.46±0.430 (S=0.3), ±0.420 (S=0.58) and ±0.519 (S=1.07).

III.   RESULTS AND DISCUSSIONS

A.   Mixture fraction distribution

Example of measured instantaneous (with resolution equal to Batchelor scale of $\approx 300 \mu m$) mixture fraction spatial distributions at different axial distances y/D_f from the burner exit for S=0.3, 0.58, 1.07 is shown in Figures 4-6. The diameter of the central pipe D_f is 15 mm, the dashed vertical line at $x/R = 0$ indicates its axis and the small vertical lines at $x/R \approx \pm 0.3$ denote the edges of the pipe. In order to gather reliable statistical results and obtain statistically stationary data, time averaging was performed for a different number of samples N (number of instantaneous images). In this work, time averaging was performed for $N = 5000$ and for $N = 1500$, which demonstrated similar results. This indicated that mixture fraction statistics were sufficiently converged for a smaller number of instantaneous images ($N = 1500$).

Instantaneous mixture fraction distribution was highly affected by the swirl number. For low swirl number of 0.3, highly non-uniform scalar field is observed for all downstream locations. For swirl numbers of 0.58 and 1.07, the distribution of mixture fraction is more homogeneous at all downstream locations.

Figures 7-9 show the spatial distribution of the time averaged (mean) mixture fraction computed from 1500 instantaneous images for S=0.3, 0.58 and 1.07. The figure shows that the flow shape is slightly non-symmetrical around the axis for S=0.58. The same slightly non-symmetrical flow shape is also found for S=1.07. As expected, the mixture fraction values were maximum close to the burner centreline and reduced with radial distance, because the scalar concentration was lower at the edge of the central jet. The mixing process was enhanced by the presence of swirl, which lead to lower scalar concentration at far away distances from the burner exit. A uniform scalar field near the centre line is observed as expected.

This slightly asymmetrical scalar distribution may be due to the weak internal recirculation zone that always exists in swirling flows with sufficiently high swirl numbers. This non-symmetrical distribution was also reported by Milosavljevic[30] and could be linked to the
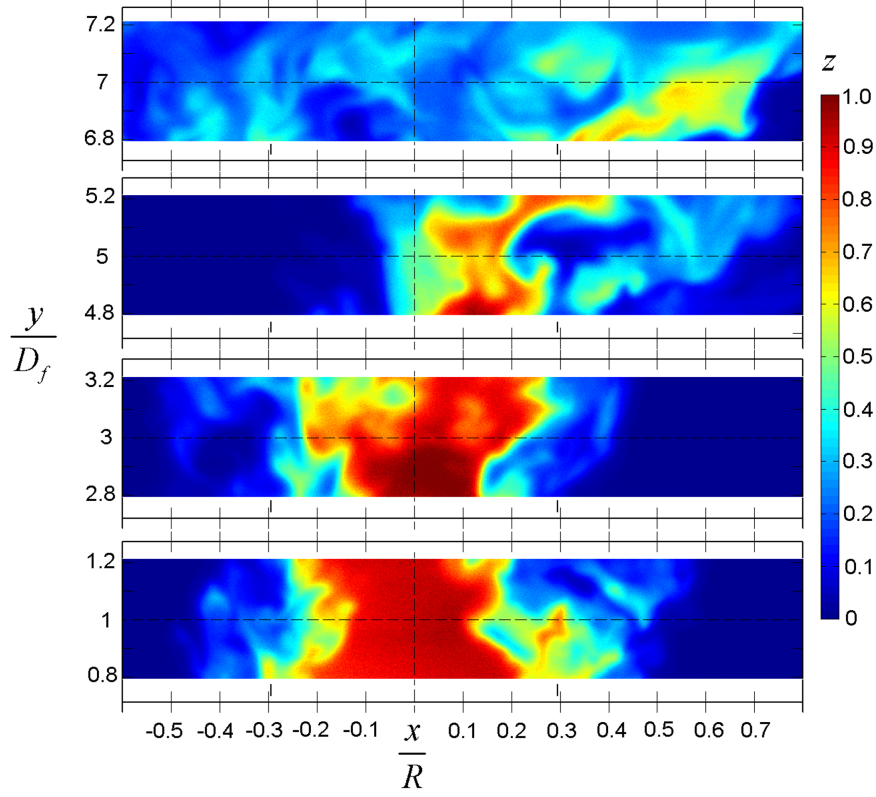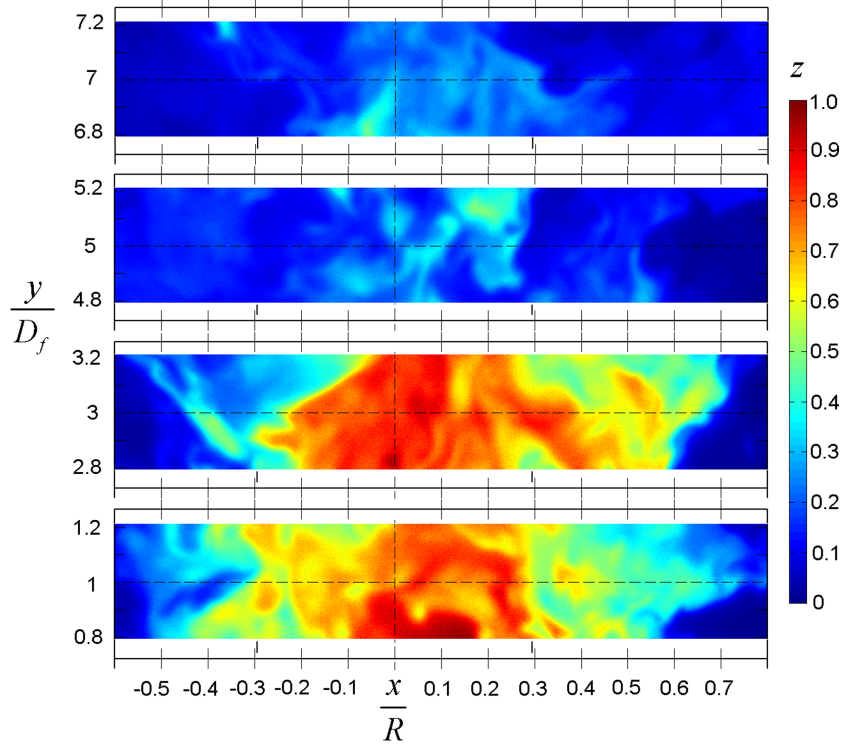
FIG. 4. Measured instantaneous mixture fraction distribution at $y/D_f = 1-7$ for annular swirl number S=0.3. Radial scale was normalised by burner radius $R = 25.4$ mm. The position of the edges of the central pipe delivering the acetone vapour jet is shown by the vertical short lines at $x/R \approx \pm 0.3$. Note that instantaneous mixture fraction distributions at different downstream positions were obtained from different realisations and are not temporally correlated.

presence of the recirculation zone, which was also supported by the velocity measurements, which were performed by Milosavljevic[30]. It is hardly unlikely that this non-symmetrical scalar distribution is due to wakes downstream three locking screws retaining the central pipe delivering the acetone vapour jet.

FIG. 5. Measured instantaneous mixture fraction distribution at $y/D_f = 1 - 7$ for annular swirl number S=0.58. Radial scale was normalised by burner radius $R = 25.4$ mm. The position of the edges of the central pipe delivering the acetone vapour jet is shown by the vertical short lines at $x/R \approx \pm 0.3$. Note that instantaneous mixture fraction distributions at different downstream positions were obtained from different realisations and are not temporally correlated.
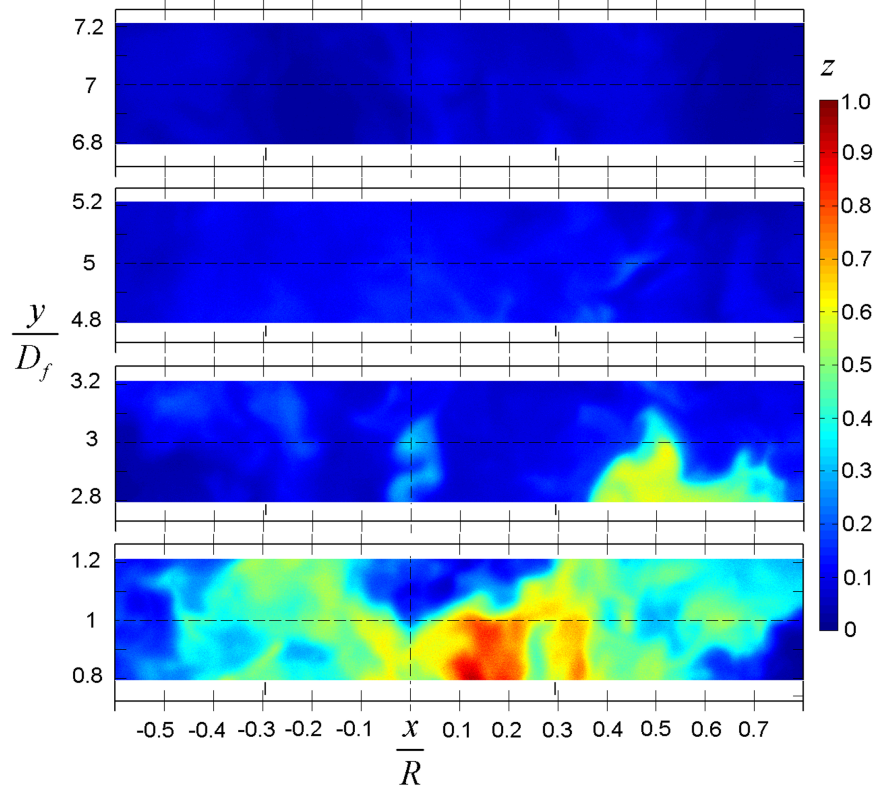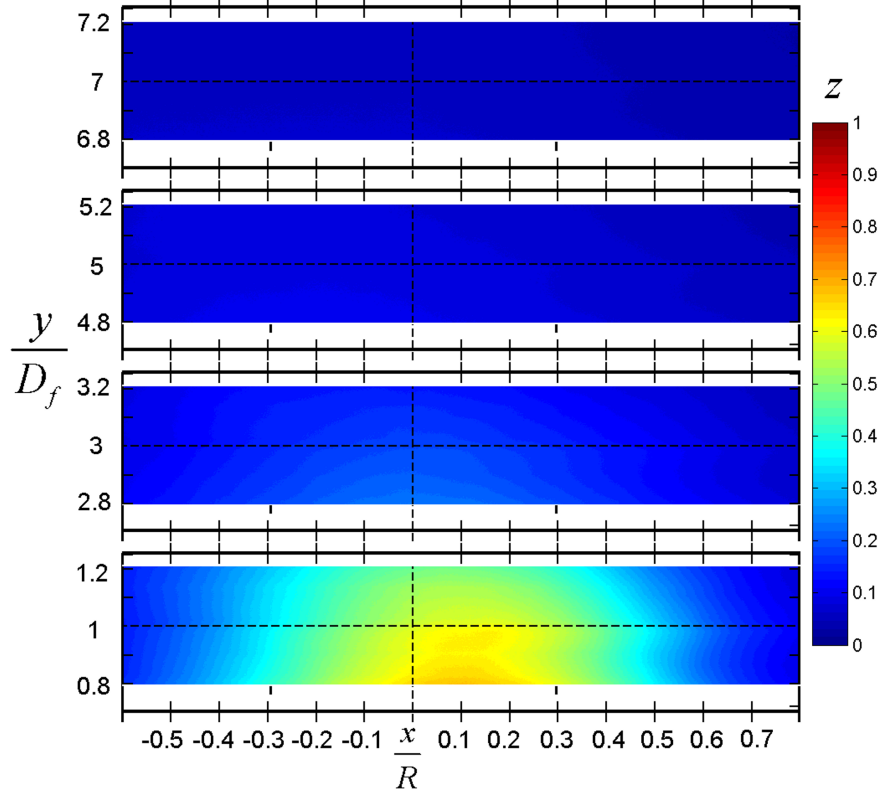
FIG. 6. Measured instantaneous mixture fraction distribution at $y/D_f = 1 - 7$ for annular swirl number S=1.07. Radial scale was normalised by burner radius $R = 25.4$ mm. The position of the edges of the central pipe delivering the acetone vapour jet is shown by the vertical short lines at $x/R \approx \pm 0.3$. Note that instantaneous mixture fraction distributions at different downstream positions were obtained from different realisations and are not temporally correlated.
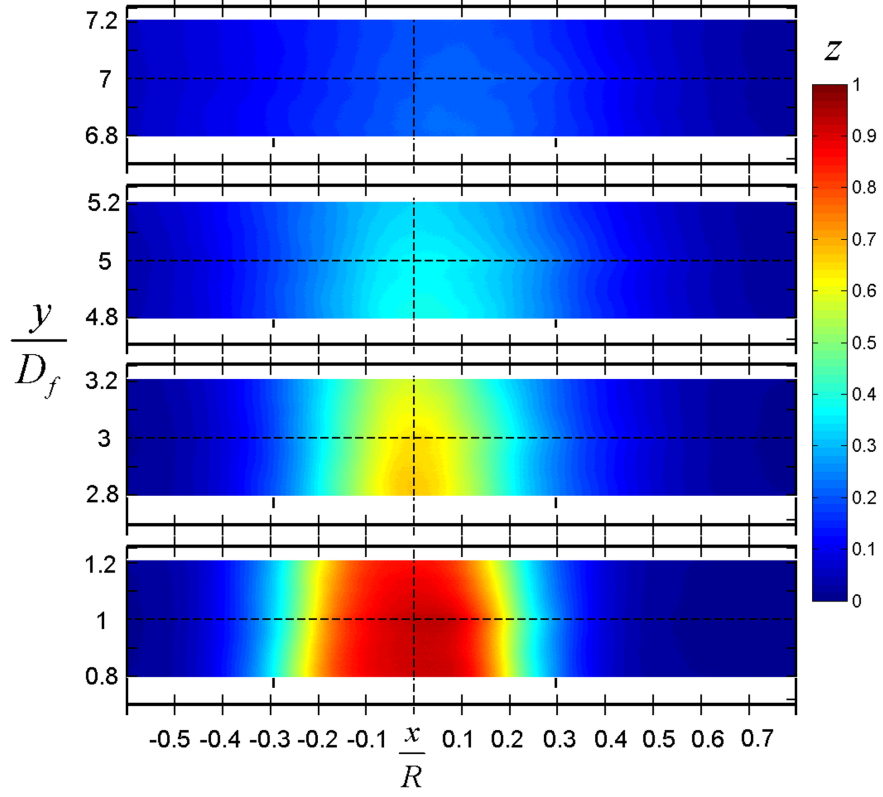
FIG. 7. Measured mean mixture fraction distribution at $y/D_f = 1 - 7$ for annular swirl number S=0.3. Radial scale was normalised by burner radius $R = 25.4$ mm. The position of the edges of the central pipe delivering the acetone vapour jet is shown by the vertical short lines at $x/R \approx \pm 0.3$.
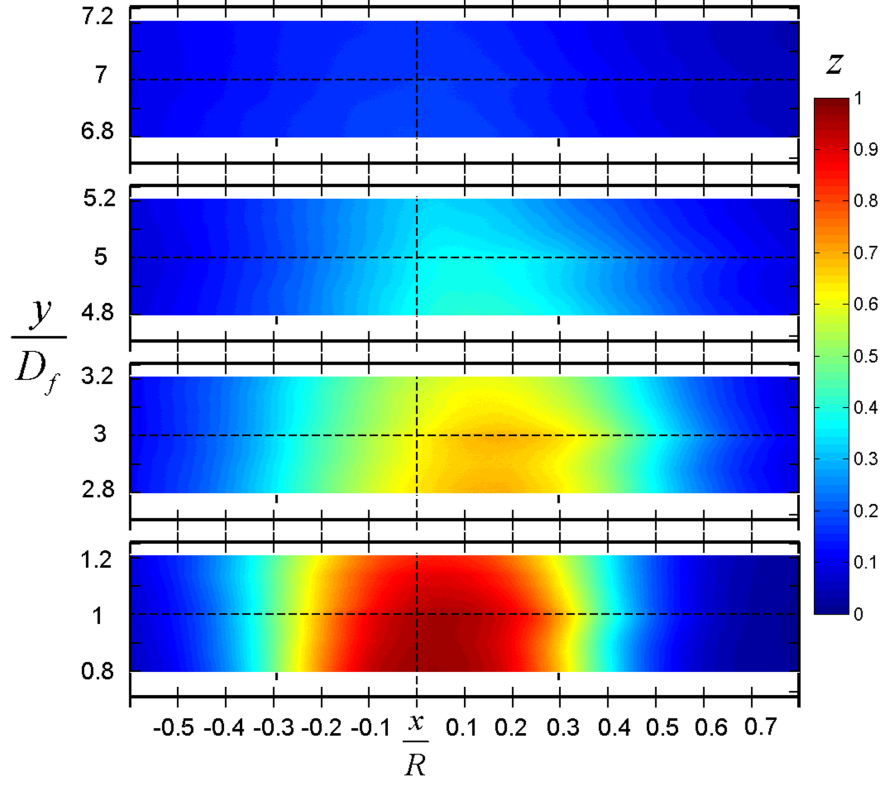
FIG. 8. Measured mean mixture fraction distribution at $y/D_f = 1 - 7$ for annular swirl number S=0.58. Radial scale was normalised by burner radius $R = 25.4$ mm. The position of the edges of the central pipe delivering the acetone vapour jet is shown by the vertical short lines at $x/R \approx \pm 0.3$. Note that slightly asymmetrical scalar distribution may be due to the weak internal recirculation zone that always exists in swirling flows with sufficiently high swirl numbers.

FIG. 9. Measured mean mixture fraction distribution at $y/D_f = 1 - 7$ for annular swirl number S=1.07. Radial scale was normalised by burner radius $R = 25.4$ mm. The position of the edges of the central pipe delivering the acetone vapour jet is shown by the vertical short lines at $x/R \approx \pm 0.3$. Note that slightly asymmetrical scalar distribution may be due to the weak internal recirculation zone that always exists in swirling flows with sufficiently high swirl numbers.
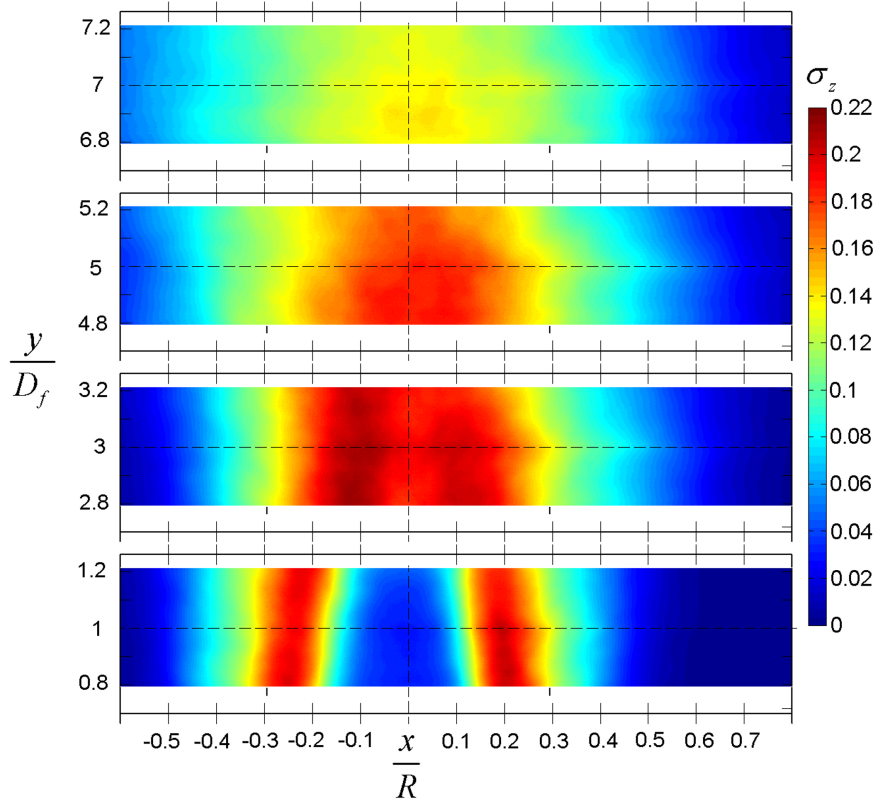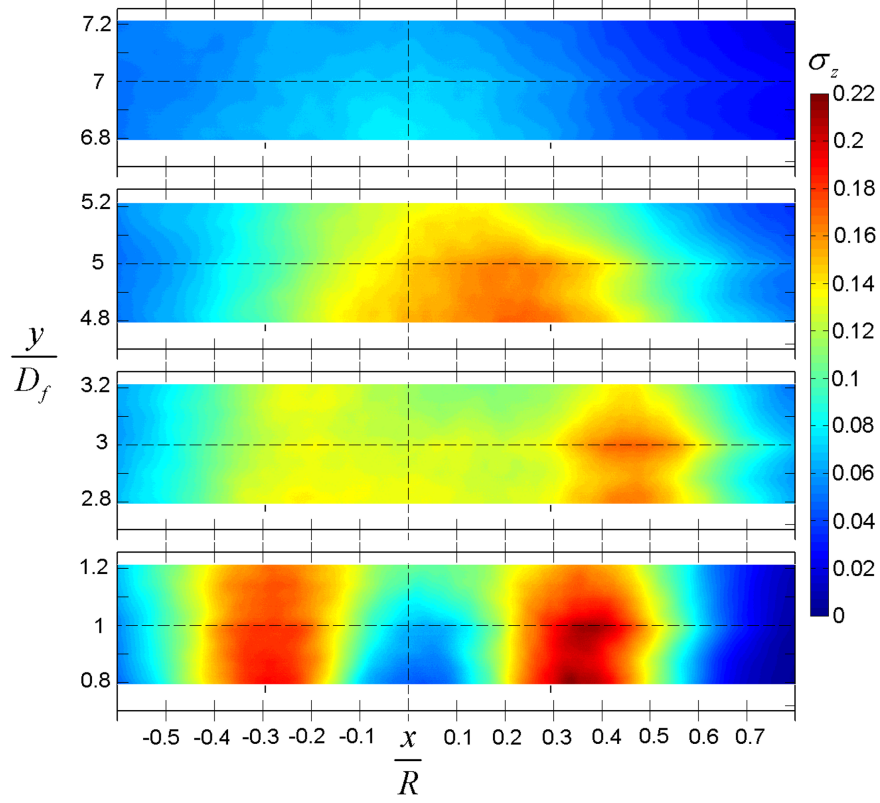
Figures 10-12 show measured standard deviation of fluctuations of mixture fraction at $y/D_f = 1 - 7$ for annular flow swirl number of 0.3, 0.58 and 1.07. A uniform distribution of low values of measured standard deviation of fluctuations of mixture fraction at $y/D_f = 7$ is clearly observed. On the other hand, at spatial locations close to the burner exit, the flow field is highly inhomogeneous, which results in high mixture fraction fluctuations. The highest values of the standard deviation of fluctuations of mixture fraction are found within the confines of the central pipe delivering the acetone vapour jet ($x/R \approx \pm 0.3$). Note that the standard deviation distribution along burner centreline $x/R = 0$ is characterized by low and approximately constant standard deviation values ($\sigma_z = 0.08\text{-}0.1$).

FIG. 10. Measured standard deviation of fluctuations of mixture fraction at $y/D_f = 1 - 7$ for annular flow swirl number S=0.3. Radial scale was normalised by burner radius $R = 25.4$ mm. The position of the edges of the central pipe delivering the acetone vapour jet is shown by the vertical short lines at $x/R \approx \pm 0.3$.
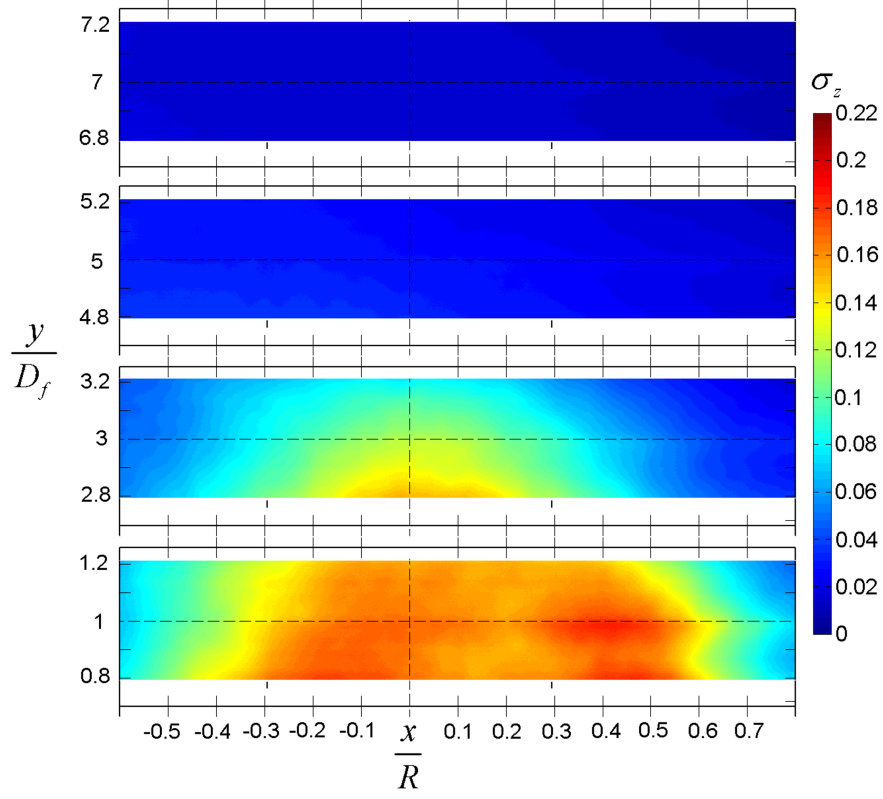
FIG. 11. Measured standard deviation of fluctuations of mixture fraction at $y/D_f = 1 - 7$ for annular flow swirl number S=0.58. Radial scale was normalised by burner radius $R = 25.4$ mm. The position of the edges of the central pipe delivering the acetone vapour jet is shown by the vertical short lines at $x/R \approx \pm 0.3$.

FIG. 12. Measured standard deviation of fluctuations of mixture fraction at $y/D_f = 1 - 7$ for annular flow swirl number S=1.07. Radial scale was normalised by burner radius $R = 25.4$ mm. The position of the edges of the central pipe delivering the acetone vapour jet is shown by the vertical short lines at $x/R \approx \pm 0.3$.

B.   Instantaneous and mean scalar dissipation rate

An example of instantaneous spatially distributed raw scalar dissipation rate (computed from raw mixture fraction image) and the result of the application of the proposed denoising procedure is shown in Figure 13. It is clearly seen that the scalar dissipation rate, which is computed from the raw mixture fraction distribution without denoising does not contain meaningful information.

Figures 14-16 show spatially distributed instantaneous scalar dissipation rate calculated after the application of the Wiener filter for S=0.3, 0.58 and 1.07, computed at different axial positions y/D_f. The maximum of instantaneous scalar dissipation rate was found to be 35 s^{-1} depending on instantaneous realization, axial position and swirl number. The general observation was that the scalar dissipation rate increased with the increase of swirl number for axial positions $y/D_f = 1, 3$ and 5. Highly non-homogeneous scalar field at lower downstream positions leads to large scalar gradients. As a result, high scalar dissipation rate is observed. Axial positions away from the nozzle exit and for highest swirl number, i.e. $y/D_f = 7$ and S=1.07, demonstrate that the scalar dissipation rate decreases to very small values due to highly homogeneous scalar fields indicating well-mixed regime, in which mixture fraction gradients are small. As it was expected, the highest scalar dissipation rate was observed at the interface between the acetone vapour jet and the annular air stream, i.e. at the radial positions of $x/R = \pm 0.3$, especially at downstream positions that are close to the nozzle exit, i.e. $y/D_f = 1, 3$ for low and intermediate swirl numbers (S=0.3, 0.58). The structure of the scalar distribution can be characterized as the thickness of the dissipation rate layers, which are seen as wrinkled flakes.

Figures 17-19 show the spatial distribution of the mean scalar dissipation rate computed from 1500 instantaneous realisations for S=0.3, 0.58 and 1.07. The values of mean scalar dissipation rate are typically much smaller than the maximum values found on instantaneous images, e.g. in Figures 14-16. The values of up to 35 s^{-1}, assuming acetone diffusivity value of 12.4 mm^2/s, can be found on instantaneous realizations, while mean values are approximately 3 s^{-1} or less. The higher mean scalar dissipation rate values correspond to lower axial positions, where the mixture fraction gradients are larger and scalar fields are highly segregated (not well mixed locally).

The highest values of the scalar dissipation rate are concentrated at the fuel jet periphery,
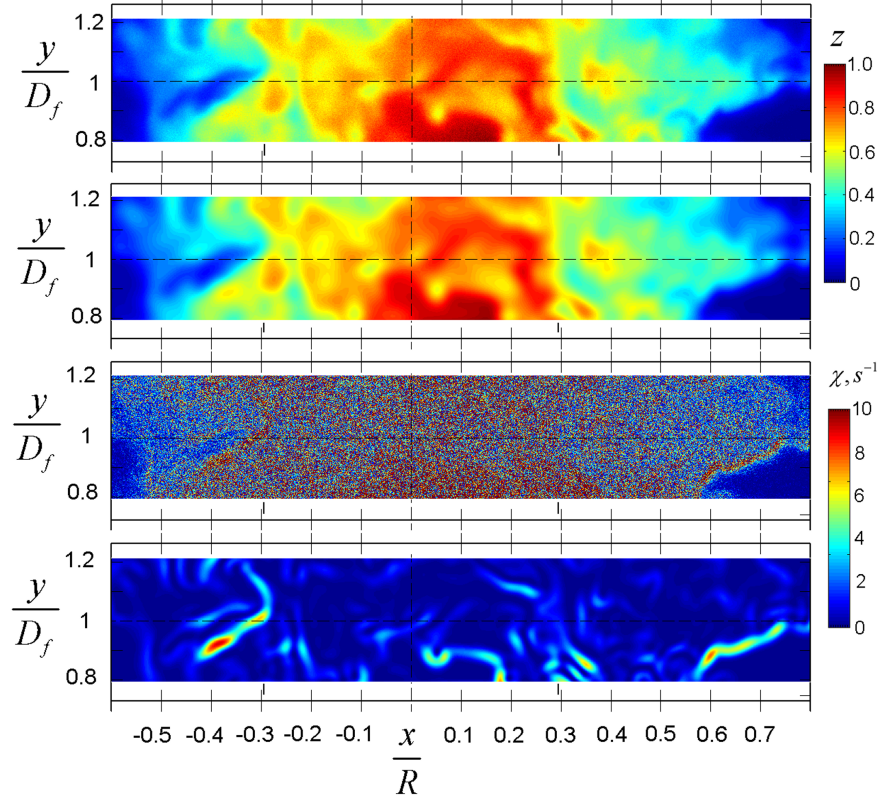
FIG. 13. Instantaneous spatially distributed scalar dissipation rate χ, s^{-1} computed from denoised and raw images at $y/D_f = 1$ for S=0.58. Radial scale was normalised by burner radius $R = 25.4$ mm. The position of the edges of the central pipe delivering the acetone vapour jet is shown by the vertical short lines at $\approx \pm 0.3$ x/R. Vertical dashed line at $x/R = 0$ is the burner centreline. From top to bottom: 1) Raw mixture fraction image; 2) Denoised mixture fraction image; 3) Scalar dissipation rate computed from raw image (1); 4) Scalar dissipation rate computed from denoised image (2).

i.e. at $x/R \approx \pm 0.3$ for $y/D_f = 1, 3$, and can be seen even on instantaneous images. However, at larger axial distances, far away from the jet origin, no distinct location of high scalar dissipation rate can be easily observed. The relatively large high-dissipation rate structures are, therefore, observed at locations where higher scalar fluctuations are found, i.e. close to the jet exit. These structures disappear with the increase of the axial distance from the jet exit.
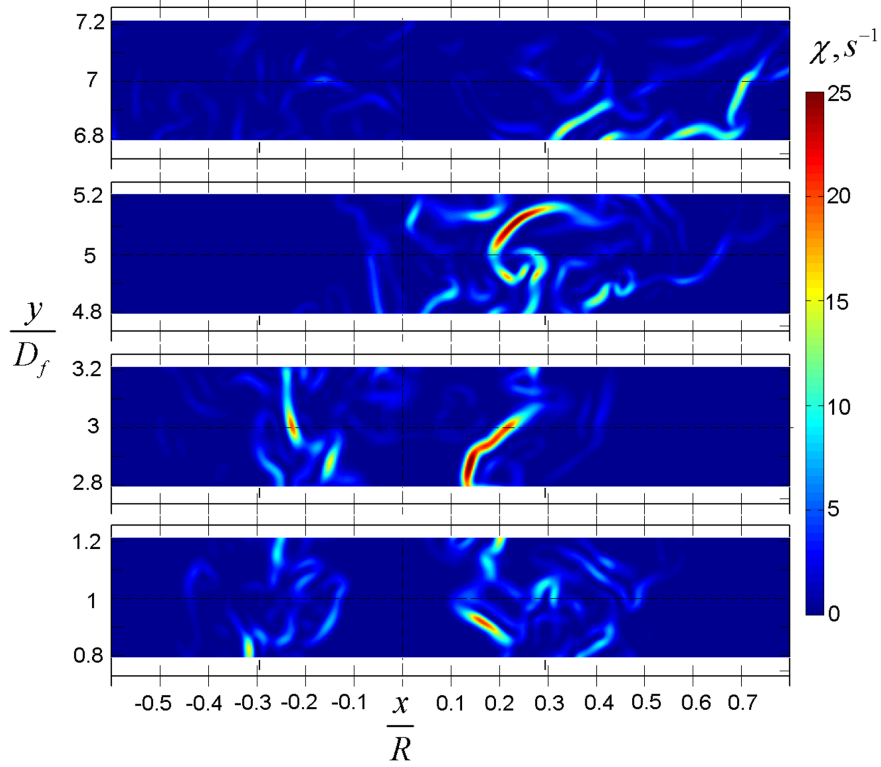
FIG. 14. Instantaneous spatially distributed scalar dissipation rate χ, s^{-1} at $y/D_f = 7, 5, 3, 1$ (from top to bottom) for S=0.3. Radial scale was normalised by burner radius R. The position of the edges of the central pipe delivering the acetone vapour jet is shown by the vertical short lines at $\approx \pm 0.3$ x/R. Vertical dashed line at $x/R = 0$ is the burner centreline. Note that the scalar dissipation rate was computed from instantaneous mixture fraction distribution shown in Figure 4.

C.   Unconditional statistics

In this section, the probability density function (p.d.f.) of the mixture fraction dissipation rate is presented. The results are useful for turbulent reacting flow models as, for example, advanced flamelet and transported p.d.f. closures, which include the fluctuations of the scalar dissipation rate. The unconditional statistics are presented in terms of the probability density functions of the scalar dissipation rate at the various positions in the flow. Window dimensions were chosen on the basis of sufficient number of samples. Five spatial locations were considered and are shown in Figure 3. Locations were chosen to represent both homogeneous and highly segregated scalar fields, i.e shear layer and centreline.
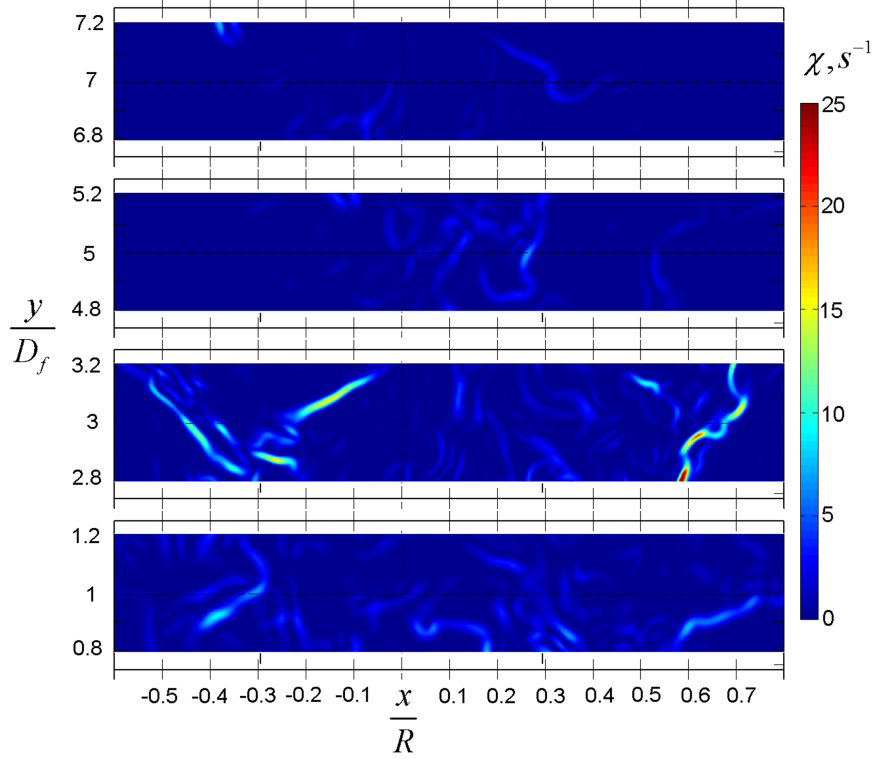
FIG. 15. Instantaneous spatially distributed scalar dissipation rate χ, s^{-1} at $y/D_f = 7, 5, 3, 1$ (from top to bottom) for S=0.58. Radial scale was normalised by burner radius R. The position of the edges of the central pipe delivering the acetone vapour jet is shown by the vertical short lines at $\approx x/R = \pm 0.3$. Vertical dashed line at $x/R = 0$ is the burner centreline. Note that the scalar dissipation rate was computed from instantaneous mixture fraction distribution shown in Figure 5.

Figures 20-22 present the p.d.f. of the fluctuations of the logarithm of the scalar dissipation rate computed from 5 windows at different axial positions for S=0.3, 0.58 and S=1.07. The p.d.fs. of the scalar dissipation rate are found to be slightly negatively skewed at low swirl number of 0.3 and almost symmetrical when the swirl number increases to 0.58-1.07. This negative skewness was also reported in a number of previous publications[19,24,25,36–38]. The assumption of a log-normal distribution of the scalar dissipation rate is usually employed in modelling of turbulent reacting flows and was also experimentally confirmed in turbulent flows[39]. Nevertheless, this assumption might be questionable and the deviations from the log-normal distribution can be observed.

We report that the probability density functions of the scalar dissipation rate are nega-
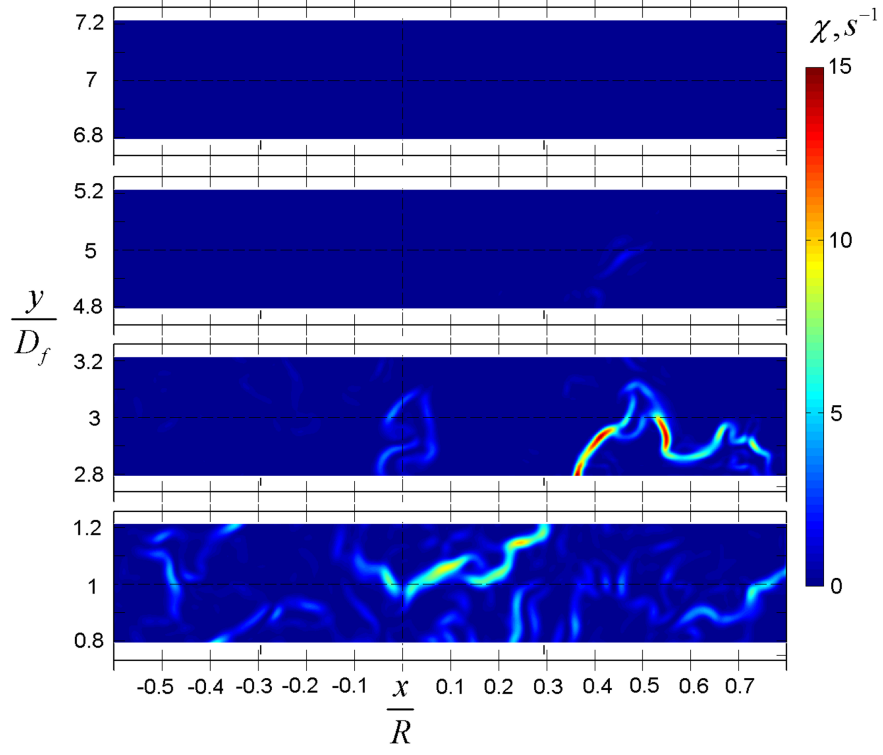
30

FIG. 16. Instantaneous spatially distributed scalar dissipation rate χ, s^{-1} at $y/D_f = 7, 5, 3, 1$ (from top to bottom) for S=1.07. Radial scale was normalised by burner radius R. The position of the edges of the central pipe delivering the acetone vapour jet is shown by the vertical short lines at $\approx x/R = \pm 0.3$. Vertical dashed line at $x/R = 0$ is the burner centreline. Note that the scalar dissipation rate was computed from instantaneous mixture fraction distribution shown in Figure 6.

tively skewed, but become almost symmetrical when a well-mixed flow regime is observed, i.e. S=1.07 at $y/D_f = 5, 7$. It is interesting to note that at swirl number of 1.07 at all axial positions and all five windows, the p.d.f. can be closely approximated by a standard log-normal distribution, i.e. with the standard deviation of 1 and a mean of 0. Therefore, it is proposed that the level of mixing directly affects the p.d.f. of scalar dissipation rate and in case of a well-mixed flow regime, i.e. far away from nozzle exit and high swirl number, only small deviation from log-normality is expected.
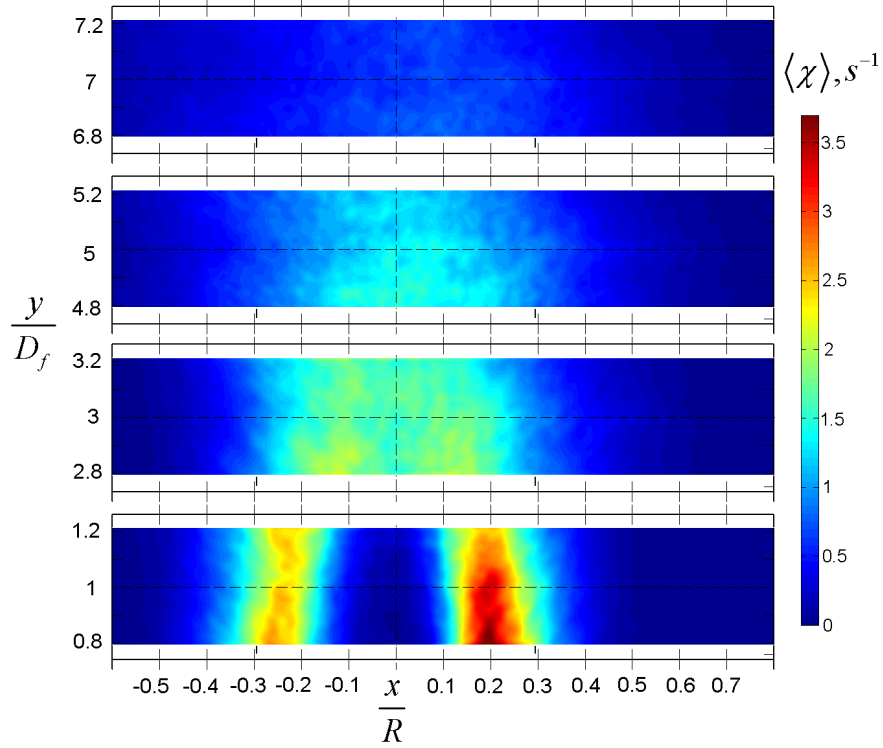
FIG. 17. Spatial distributions of mean scalar dissipation rate $\langle \chi \rangle$, s^{-1} computed from 1500 images at $y/D_f = 7, 5, 3, 1$ (from top to bottom) for S=0.3. The position of the edges of the central pipe delivering the acetone vapour jet is shown by the vertical short lines at $x/R \approx \pm 0.3$. Vertical dashed line at $x/R = 0$ is the burner centreline.

D. Joint statistics between scalar and its dissipation rate

This section quantifies the departures from statistical independence of the scalar fluctuations and their dissipation rate by comparing the joint p.d.f. of scalar and its dissipation rate with the product of the individual p.d.fs. of scalar and dissipation rate. The joint p.d.f. is the association of the mixture fraction fluctuations with the fluctuations of the scalar dissipation rate. In modelling of turbulent reacting flows, it is usually assumed the statistical independence between the scalar fluctuations and their dissipation rate. This approximation has not yet been evaluated experimentally in swirling flows. The statistical independence assumption means that the joint p.d.f. is equal to the product of the individual p.d.fs.

In statistics, the dependence of two random variables or two data sets can be assessed by the so-called correlation coefficient. If any two random variables are independent, the correlation coefficient is zero. On the other hand, if the correlation coefficient is zero it
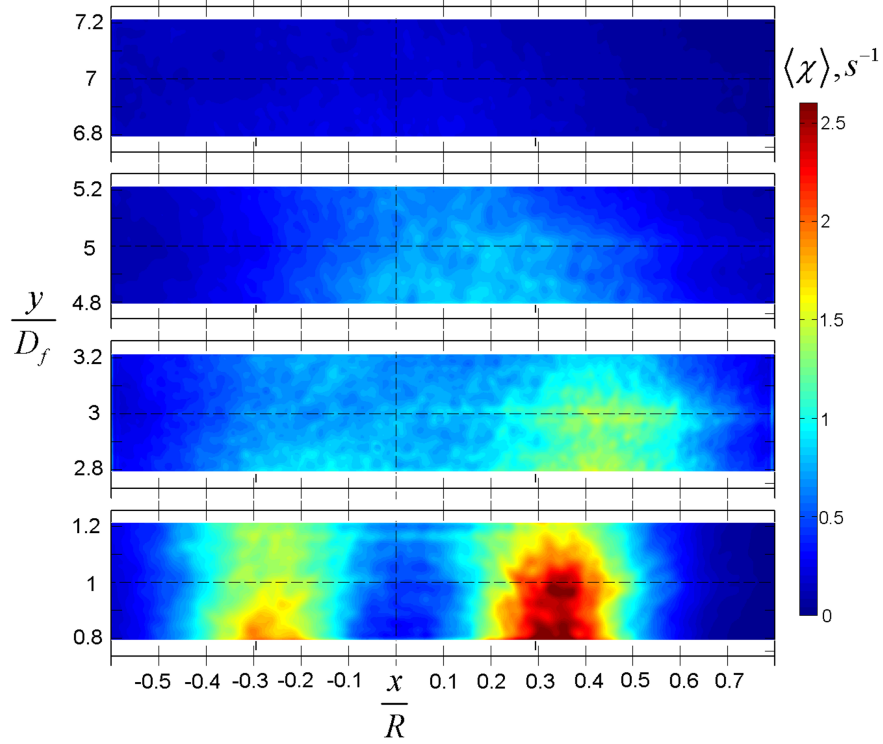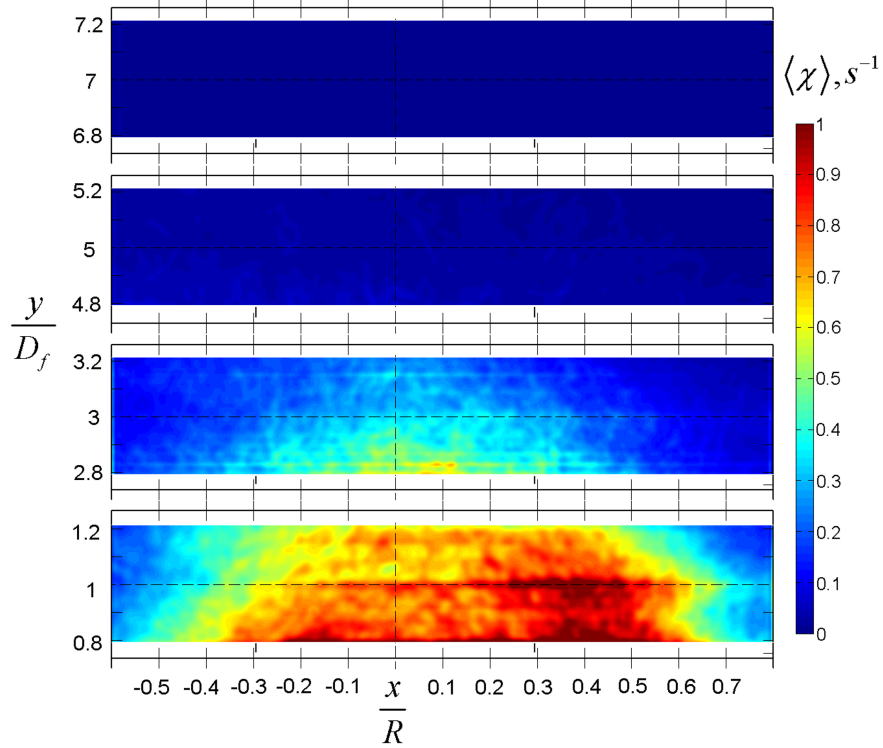
FIG. 18. Spatial distributions of mean scalar dissipation rate $\langle \chi \rangle, s^{-1}$ computed from 1500 images at $y/D_f = 7, 5, 3, 1$ (from top to bottom) for S=0.58. The position of the edges of the central pipe delivering the acetone vapour jet is shown by the vertical short lines at $x/R \approx \pm 0.3$. Vertical dashed line at $x/R = 0$ is the burner centreline.

does not guarantee that the two random variables are statistically independent, because the coefficient detects only linear dependencies between the two variables. The correlation coefficient or Pearson's correlation coefficient when applied to a sample is commonly defined as the sample correlation coefficient according to the following equation, where z and χ are the mixture fraction and its dissipation rate. The correlation coefficient ranges from -1 to +1. If the correlation coefficient of the scalar fluctuations and the scalar dissipation rate is zero, the scalar and its dissipation rate is not necessarily statistically independent. For non-zero values of correlation coefficient the scalar fluctuations and the scalar dissipation rate are statistically related[40].

FIG. 19. Spatial distributions of mean scalar dissipation rate $\langle\chi\rangle$, s^{-1} computed from 1500 images at $y/D_f = 7, 5, 3, 1$ (from top to bottom) for S=1.07. The position of the edges of the central pipe delivering the acetone vapour jet is shown by the vertical short lines at $x/R \approx \pm 0.3$. Vertical dashed line at $x/R = 0$ is the burner centreline. The values of mean scalar dissipation rate at $y/D_f = 5, 7$ are circa 0.01 and uniformly distributed.

$$r_{z,\chi} = \frac{\sum_{i=1}^{N} (z_i - \bar{z})(\chi_i - \bar{\chi})}{\sqrt{\sum_{i=1}^{N}(z_i - \bar{z})^2}\sqrt{\sum_{i=1}^{N}(\chi_i - \bar{\chi})^2}} \tag{13}$$

In general, the correlation coefficient can serve as an initial estimator of statistical independence and further investigation by comparing the joint p.d.f. to the product of the individual p.d.fs. is usually required.

Pearson's correlation coefficients are shown in Figure 23 as a function of axial distances and window locations for two swirl numbers of 0.58 and 1.07. Non-zero correlation coefficients are direct indicators that the scalar and its dissipation rate are statistically related. However, the relationship between the scalar and its dissipation rate is not linear and is also
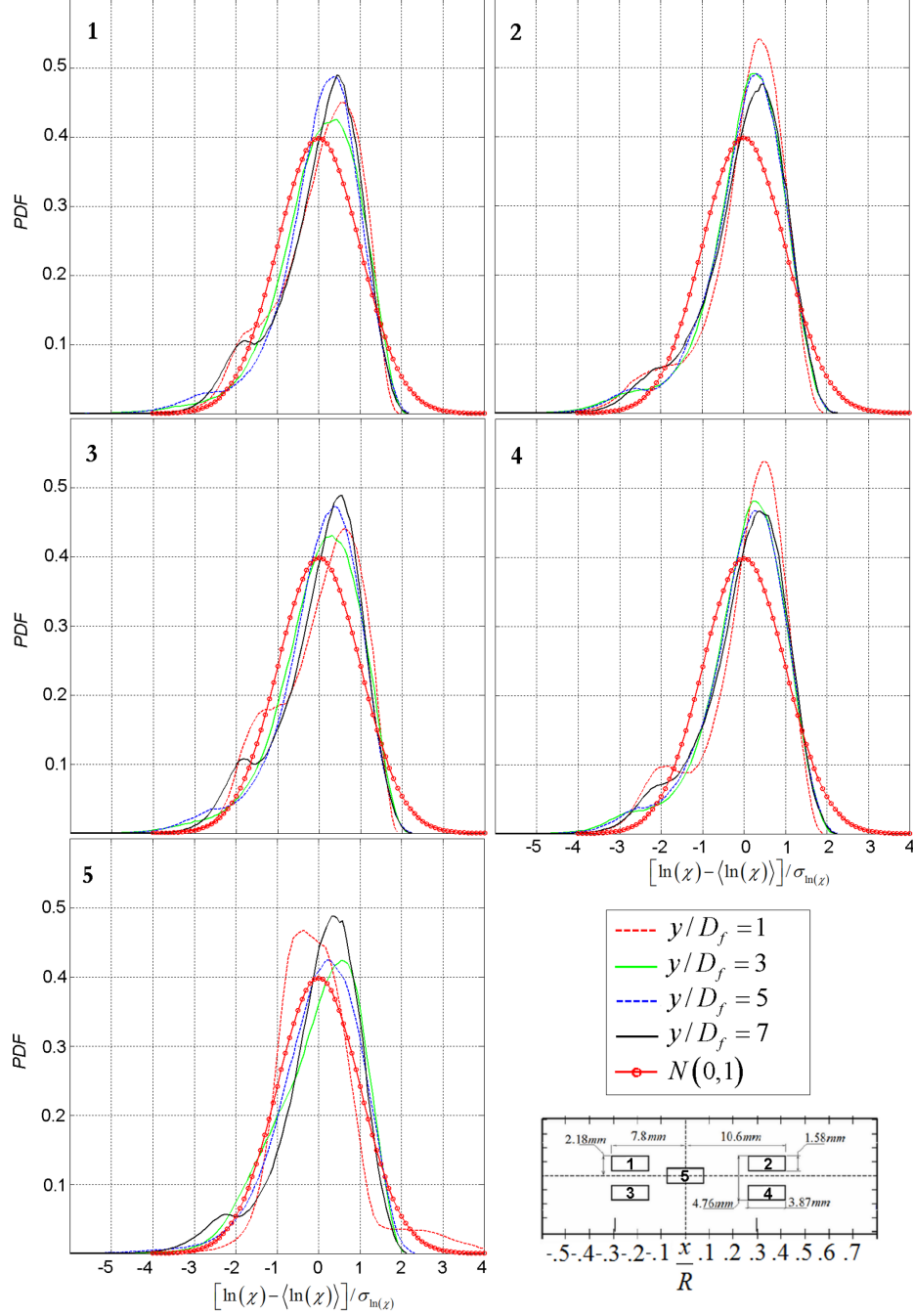
FIG. 20. The p.d.fs. of the fluctuations of the logarithm of the scalar dissipation rate from windows 1-5, computed at $y/D_f = 1, 3, 5, 7$ for S=0.3. Gaussian function with expected value of 0 and standard deviation of 1 is also shown in each plot. Corresponding window numbers are shown in top left corner of each plot. Window dimensions are 1.58 mm $\times$ 3.87 mm $(\approx 4\lambda_\beta \times 10\lambda_\beta)$ and their locations are shown in bottom right corner and in Figure 3.

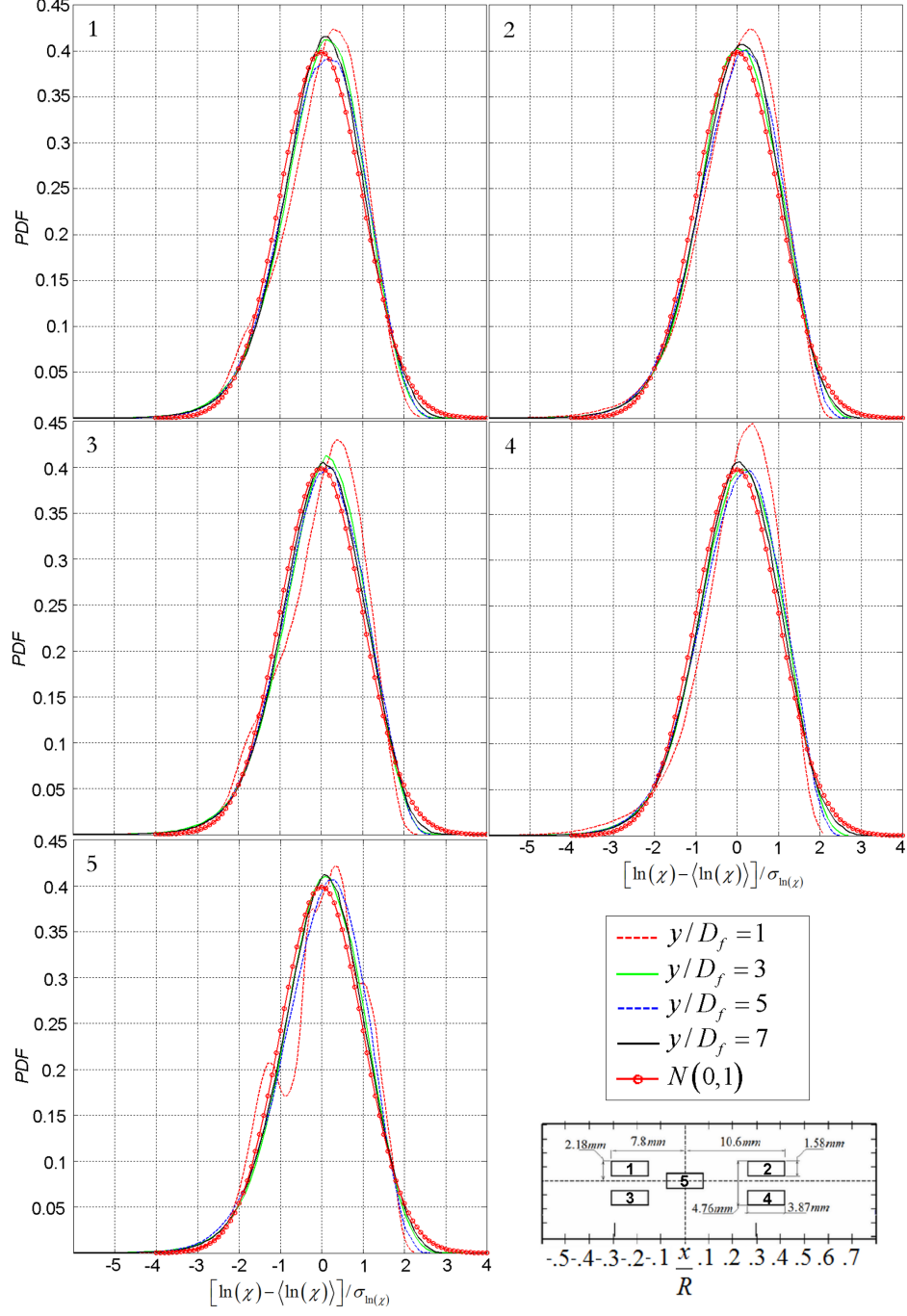dependent on windows positions. In addition, the statistical dependence is rather week for

FIG. 21. The p.d.fs. of the fluctuations of the logarithm of the scalar dissipation rate from windows 1-5, computed at $y/D_f = 1, 3, 5, 7$ for S=0.58. Gaussian function with expected value of 0 and standard deviation of 1 is also shown in each plot. Corresponding window numbers are shown in top left corner of each plot. Window dimensions are 1.58 mm $\times$ 3.87 mm ($\approx 4\lambda_\beta \times 10\lambda_\beta$) and their locations are shown in bottom right corner and in Figure 3.

high swirl number. If the assumption of independence between the scalar fluctuations and the scalar dissipation rate is valid, then by definition the joint probability distribution of the scalar fluctuations and their dissipation rate will be equal to the product of the individual p.d.f. In this work, the joint p.d.f. was computed from the logarithm of the instantaneous values of the scalar dissipation rate minus the mean of the logarithm of the scalar dissipation rate, normalized by the standard deviation of the logarithm of the scalar dissipation rate and from the instantaneous values of the mixture fraction minus the mean of the mixture fraction, normalized by the standard deviation of the mixture fraction fluctuations. The join p.d.f. was computed by using 50 two-dimensional bins. In Figures 24-25 of joint p.d.f., the x and the $y-$axes are plotted according to the following equations.

$$x - Axis = \frac{\ln\left(\chi\right) - \langle\ln\left(\chi\right)\rangle}{\sigma_{\ln(\chi)}} \tag{14}$$

$$y - Axis = \frac{z - \langle z\rangle}{\sigma_z} \tag{15}$$

Figures 24-25 can assess the assumption of statistical independence. These plots are arranged in two columns, where left column corresponds to the joint p.d.f. of the scalar and its dissipation rate, while right column corresponds to the product of individual p.d.fs. of the scalar and its dissipation rate. The plotting range was the same for all plots and ranged from -4 to +4 standard deviations. The product of two p.d.fs. was computed by using the same bin number as in the joint p.d.f. The joint p.d.f. and the product of the p.d.fs. were plotted by using 20 contour lines.

At all five window locations (only one location is shown here) at $y/D_f = 1$ and for S=1.07 the contours of the product of the individual p.d.fs. appear close to circular, even though not entirely symmetric (Figure 25). The joint p.d.f. has an oval shape and appears to be skewed towards both negative and positive dissipation rate fluctuations. The centre of the joint p.d.f. and the product of individual p.d.fs. seem to have the same origin. The assumption of statistical independence is therefore in better agreement with the experimental data at regimes of homogeneous scalar field or well-mixed regime. However, deviations from the assumption of statistical independence are clearly observed, where the scalar is not homogeneous and large scalar fluctuations are present.

The joint p.d.f. for low swirl number (Figure 24) is skewed towards negative values

of scalar dissipation rate with large negative fluctuations of mixture fraction, while the product of the individual p.d.fs. sometimes displays bimodal features. This can be due to large sampling window and jet flapping effect. However, the bimodal p.d.fs were observed even for smaller filter sizes[41]. Therefore, the assumption of statistical independence is not held, since the two shapes are quite different and vary with location.

In fact, the product of the individual p.d.fs. reproduces the probability of occurrence of values lower than the mean, i.e. large negative fluctuations, even though the shape is quite different from that of the joint p.d.f. In addition, the joint p.d.f. demonstrates that intermittency plays an important role and can affect the shape of the p.d.f., even though not much, which is not accounted by the product of individual p.d.fs. The intermittency causes the joint p.d.f. to be skewed towards negative values of the logarithm of scalar dissipation rate.

Preliminary conclusions on statistical independence of the scalar fluctuations and the scalar dissipation rate in swirling flows are summarized as follows: The scalar fluctuations were strongly correlated at the boundaries of the mixing layer or shear layer, especially for low swirl numbers. The assumption of statistical independence between the scalar fluctuations and their dissipation rate, commonly introduced in modelling of turbulent reacting flows was, therefore, not tenable for low swirl numbers.

On the other hand, the assumption of statistical independence between the scalar fluctuations and their dissipation rate was justified in case of high swirling flows (S>0.6). It was also found that the skewness of the joint p.d.f. was dependant on the swirl number as well as on the intermittency. The intermittency was not found when the swirl number was large, namely 1.07, and the shape of the contours of the joint p.d.f. was then close to circular.

The joint p.d.f. gives the measure of the joint probability between scalar fluctuations and their dissipation rate, even though does not provide a physical explanation for the processes that give rise to the correlation between the scalar fluctuations and their dissipation rate. This can give the conditions under which the assumption of statistical hypothesis breaks down. This is useful information, but incomplete, because it is unknown which components contribute more, i.e. axial or radial components of scalar dissipation rate. The contribution of each part of the scalar fluctuations and the scalar dissipation rate to their overall correlation can be understood by using a weighting function. The weighting function $w\left(z, \ln\left(\chi\right)\right)$ is defined as product of mixture fraction z, logarithm of the scalar

dissipation rate and their joint p.d.f. so that the double integral over scalar fluctuations and the dissipation rate is the correlation coefficient[19,24]. This is demonstrated in equations (11)-(14).

$$w\left(z', \chi'\right) = z' \chi' pdf\left(z', \chi'\right) \tag{16}$$

$$r_{z', \chi'} = \int\limits_{-\infty}^{\infty} \int\limits_{-\infty}^{\infty} z' \chi' pdf\left(z', \chi'\right) \tag{17}$$

$$z' = \frac{z - \bar{z}}{\sigma_z} \tag{18}$$

$$\chi' = \frac{\ln\left(\chi\right) - \overline{\ln\left(\chi\right)}}{\sigma_{\ln(\chi)}} \tag{19}$$

It is also possible to assess the relative importance of the axial, radial or both components of the scalar dissipation rate to the overall correlation by computing the weighted integrands from single components of the scalar dissipation rate (axial or radial). This approach provides a rapid overview of identifying the origin of the correlation between the scalar and its dissipation rate. The weighted integrands computed from both axial and radial components of the joint p.d.f. and radial component only are presented in Figure 26 for S=1.07 at $y/D_f = 1$ computed from window 2. The weighted integrands from both components (radial and axial) of the scalar dissipation rate demonstrated that correlations were primarily from large negative scalar dissipation rate fluctuations, which tend to be rare events but have very large contribution.

Figure 27 shows the weighted integrands computed from axial and radial components of the scalar dissipation rate for window 2 by using the joint p.d.f. at $y/D_f = 1$ for S=0. For the flow conditions without swirling motion, i.e. for S=0 (acetone vapour jet only), the radial and axial components contribute almost equally to the overall correlation. The contribution of radial component increases, as the level of mixing increases, which is illustrated in Figure 28. A general conclusion is that in swirling flows the contribution from the axial and the radial component of the scalar dissipation rate is not equal and is directly related to the degree of mixing, i.e. the swirl number. It could be assumed that for a certain swirl number (0<S<1.07), the contribution from axial and radial components to the overall correlation would be equal.
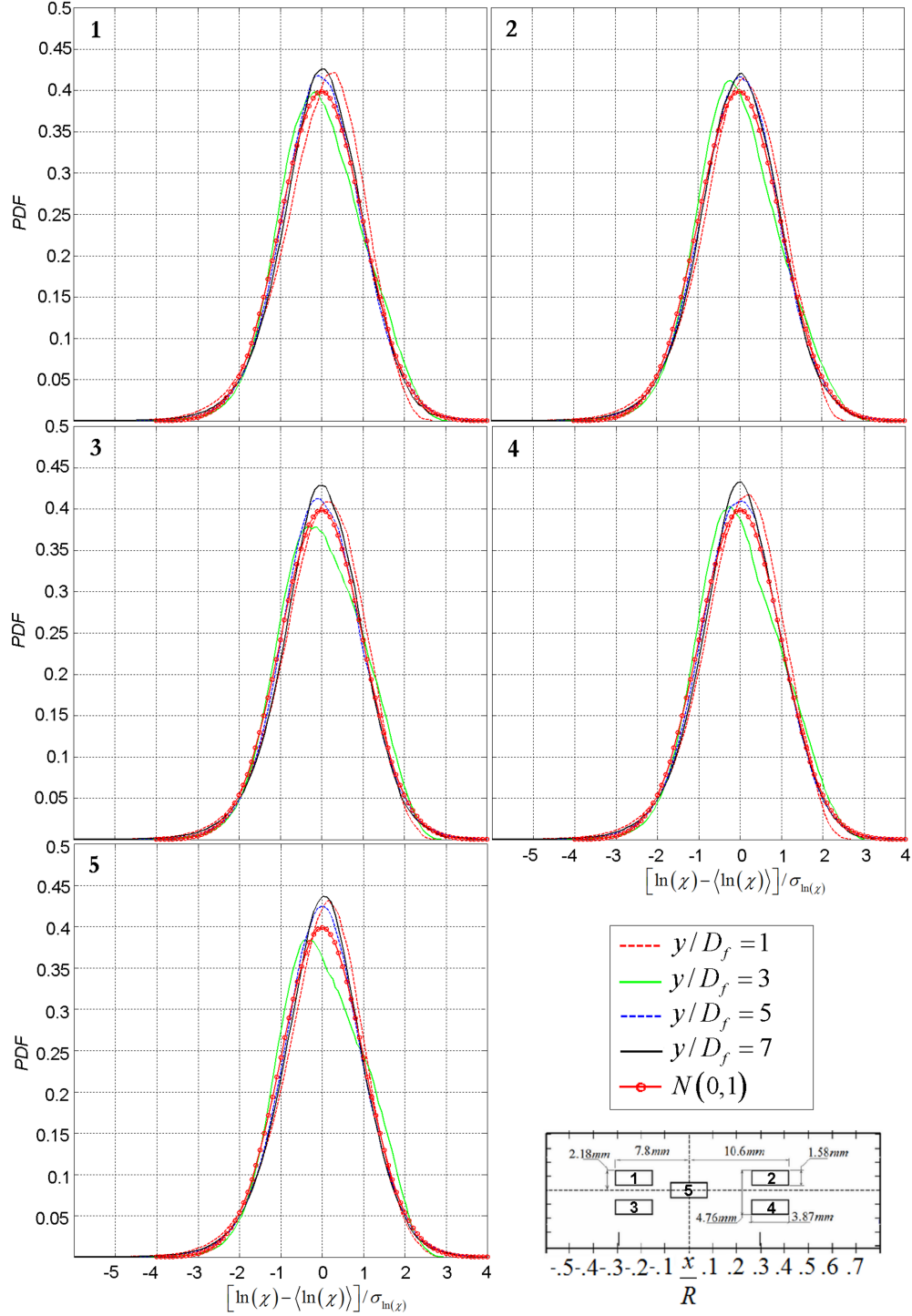
FIG. 22. The p.d.fs. of the fluctuations of the logarithm of the scalar dissipation rate from windows 1-5, computed at $y/D_f = 1, 3, 5, 7$ for S=1.07. Gaussian function with expected value of 0 and standard deviation of 1 is also shown in each plot. Corresponding window numbers are shown in top left corner of each plot. Window dimensions are 1.58 mm $\times$ 3.87 mm ($\approx 4\lambda_\beta \times 10\lambda_\beta$) and their locations are shown in bottom right corner and in Figure 3.
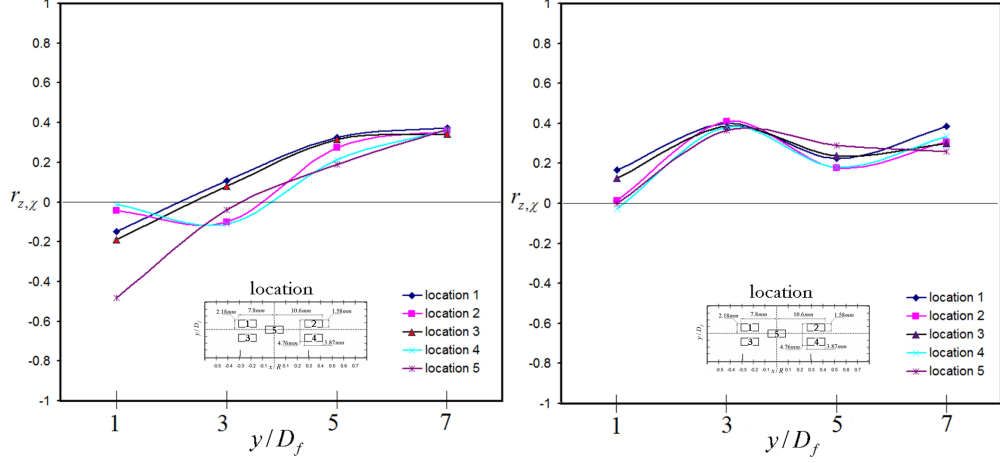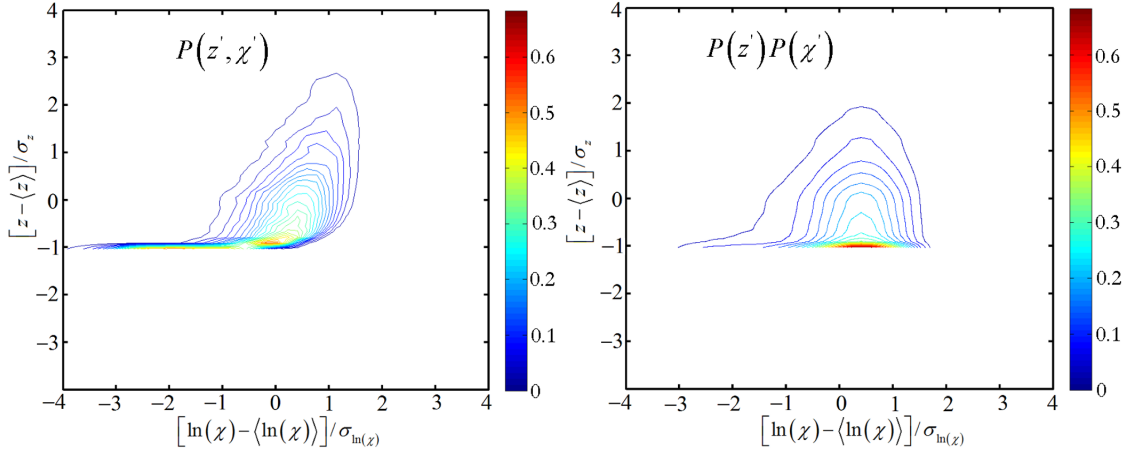
FIG. 23. Pearson's correlation coefficients of the scalar and its dissipation rate as a function of axial distances and window locations for S=0.58 (left) and S=1.07 (right). Window dimensions are 1.58 mm × 3.87 mm ($\approx 4\lambda_\beta \times 10\lambda_\beta$) and their locations are shown in Figure 3.
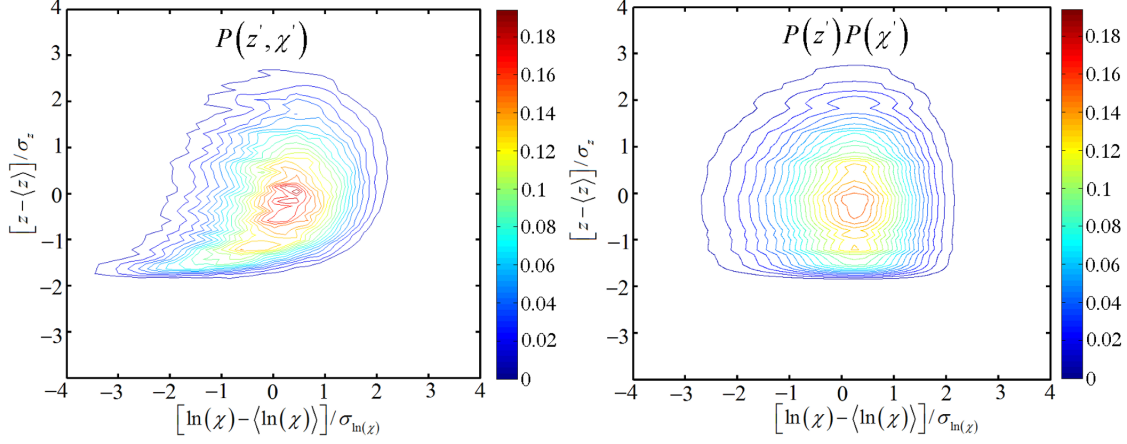

FIG. 24. Joint p.d.f. of the scalar and its dissipation rate (left) and the product of individual p.d.f. (right) at $y/D_f = 1$ for S=0.3, computed for window 2. Plotting range is ±4 standard deviations. Other window sizes demonstrate similar trend.

FIG. 25. Joint p.d.f. of the scalar and its dissipation rate (left) and the product of individual p.d.f. (right) at $y/D_f = 1$ for S=1.07, computed for window 1. Plotting range is ± 4 standard deviations. Other window sizes demonstrate similar trend.
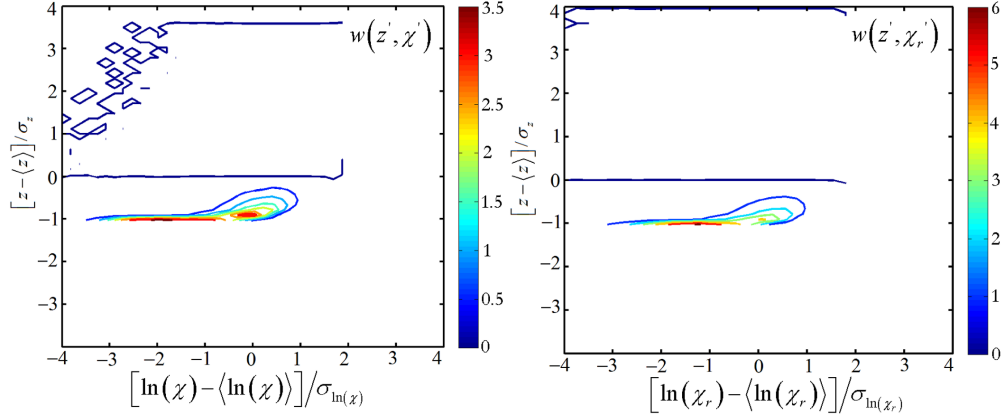

FIG. 26. The weighted integrands computed from both axial and radial components of the scalar dissipation rate (left) and the radial component only (right) for window 2 by using the joint p.d.f. at $y/D_f = 1$ for S=1.07. Note that radial component contributes more, which is indicated by maximum value shown on the colorbar.
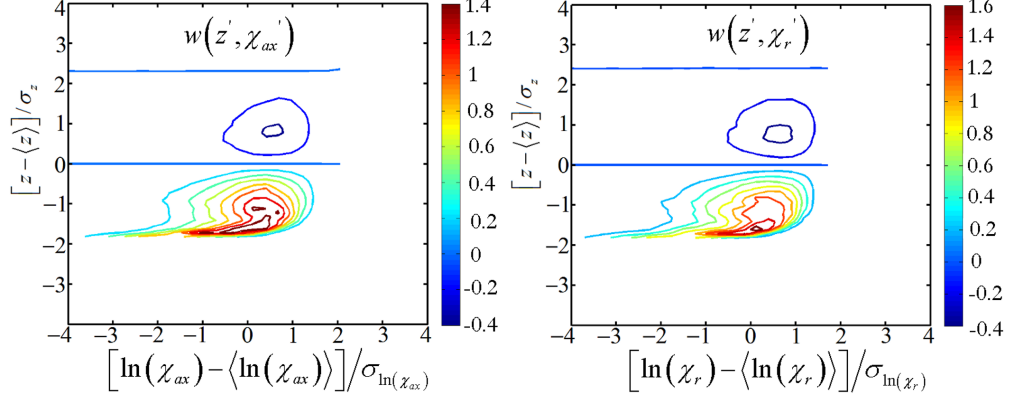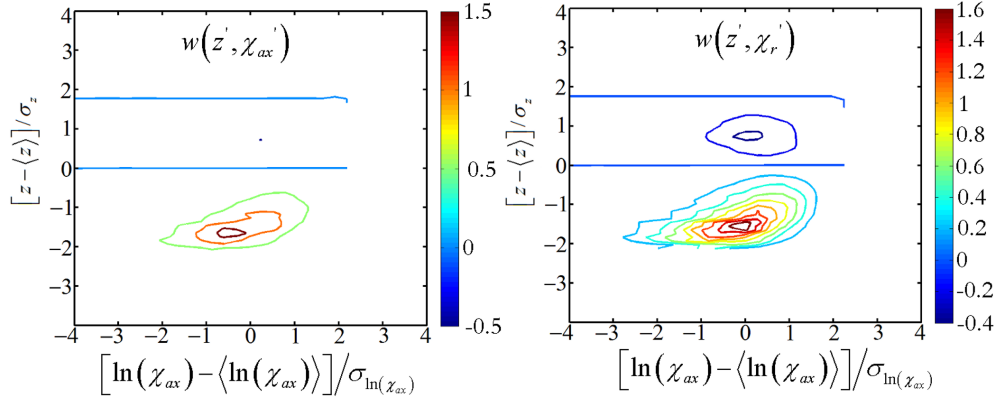
FIG. 27. The weighted integrands computed from axial (left) and radial components (right) of the scalar dissipation rate for window 2 by using the joint p.d.f. at $y/D_f = 1$ for S=0 (no swirling co-flow). Note that almost equal contribution from axial and radial components is observed.

FIG. 28. The weighted integrands computed from axial (left) and radial components (right) of the scalar dissipation rate for window 2 by using the joint p.d.f. at $y/D_f = 1$ for S=1.07.

E. Conditional scalar dissipation rate

The conditional statistics of the scalar dissipation rate were computed by dividing the mixture fraction space in a number of bins, of typical width less than 0.01 mixture fraction values and a typical size of 150000 samples in each bin. Averaging takes place in each bin so that the conditional mean of the scalar dissipation rate is computed. Similarly, the conditional standard deviation is computed from the data in each bin. Typically, 110 equally spaced bins were used to split the mixture fraction space containing 12e6 values, which resulted in 107000-280000 samples in each bin (depending on the bin number). Therefore, the statistical uncertainty is negligible.

The conditional mean of the scalar dissipation rate for S=0.3, 0.58 and 1.07 is shown in Figures 29-31. Standard deviation of scalar dissipation rate conditional on mixture fraction is shown in Figures 32-34. The conditional mean and the standard deviation of the scalar dissipation rate have a well-defined hyperbolic-shaped structure in the mixture fraction space, which is well-known from the measurements in non-swirling flows. General observation of the mean scalar dissipation rate reveals that the mean increases with the mixture fraction, reaching a maximum value, then gradually decreases and reaches zero. With increasing swirl number the conditional mean decreases and its maximum values shift to lower mixture fraction values. The conditional mean also shifts to lower mixture fraction values with higher axial distances y/D_f.

The location of the maximum conditional mean shifts from 0.6 mixture fraction units for S=0.3, 0.4 units for S=0.58 and 0.3-0.4 units for the highest swirl number of 1.07. For lower swirl numbers, the conditional mean has clearly visible smooth shape, which somehow resembles a bell curve, while, for higher swirl number and higher degree of mixing, the conditional mean is converging to delta function. The variation of the conditional mean is consistent with the fact that the mean approaches zero at large and small mixture fraction values. This is due to the fact that larger and smaller mixture fraction values correspond to either jet fluid or ambient fluid, where scalar gradients are zero. The weighted probability of occurrence of the mean conditional scalar dissipation rate for S=0.3 is shown in Figure 35. The weighted probability of occurrence of the mean conditional scalar dissipation coincides with the conditional mean of the scalar dissipation rate and, hence, is presented for S=0.3 only[42].

The standard deviation of the scalar dissipation rate conditioned on the mixture fraction demonstrates similar trends as the conditional mean with similar bell-shaped curve. The maximum values of the standard deviation attain maximum at the same mixture fraction units as the conditional mean. Even though the peak of the standard deviation of the scalar dissipation rate is approximately constant irrespective of swirl number, the form of the distribution is dependant on the swirl number. The distribution of the standard deviation follows the conditional mean pattern and for high swirl numbers becomes 'sparse scattered' (Figure 34 windows 2 and 4).

In addition, the conditional probability density function of the scalar dissipation rate, evaluated for an arbitrary mixture fraction value of 0.3, is presented here (Figure 36). Conditional probabilities for other z demonstrate similar trend. The conditional p.d.fs. were evaluated from the logarithm of the scalar dissipation rate minus the mean of the logarithm of the scalar dissipation rate, normalized by the standard deviation of the logarithm of the scalar dissipation rate. The conditional and unconditional p.d.fs. are very similar with small deviation from log-normal distribution and large negative fluctuations around the mean. Similar observations of the conditional p.d.f have been made for other values of the scalar dissipation rate and the conclusions can be extended to all mixture fraction units independent of swirl number.
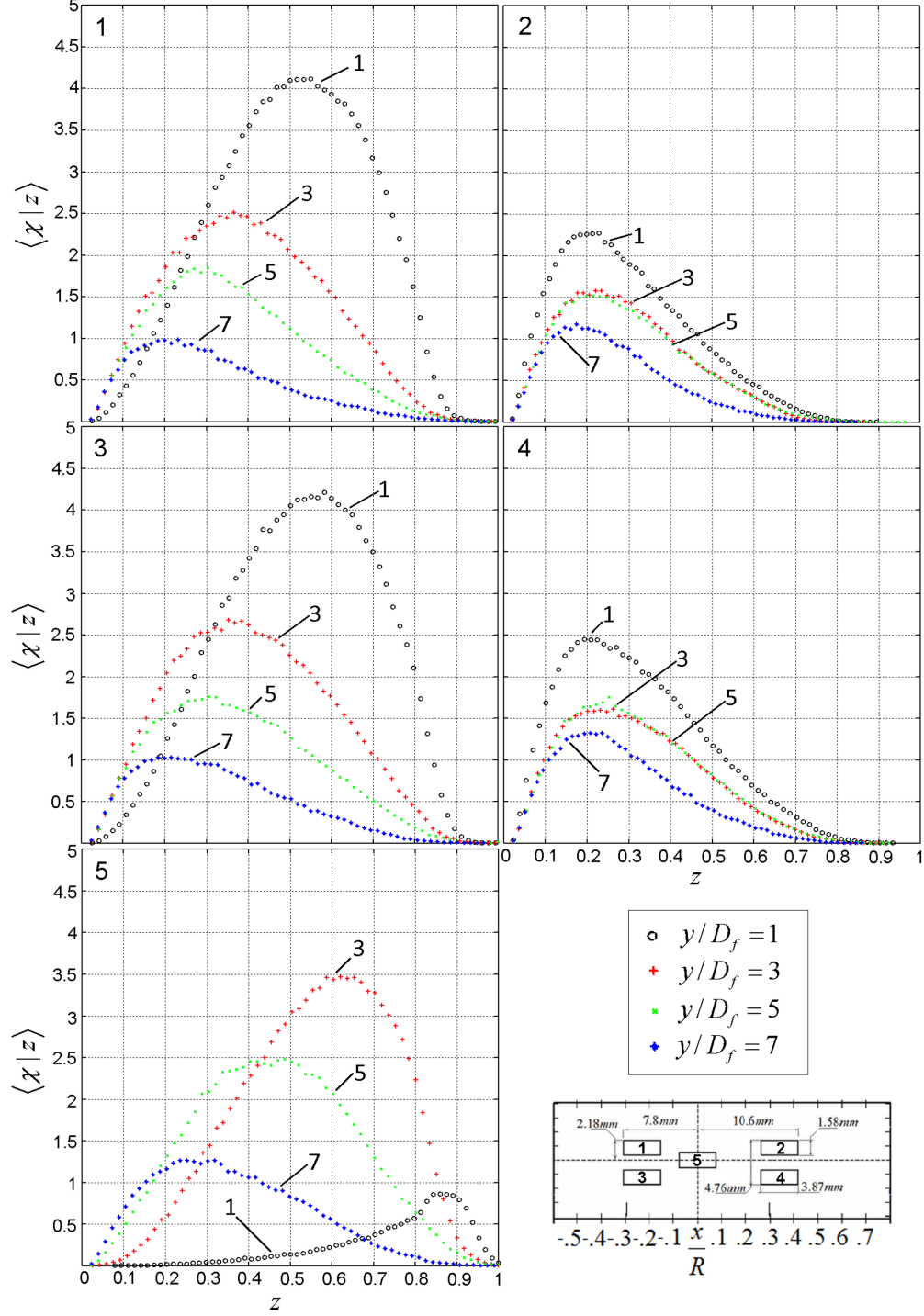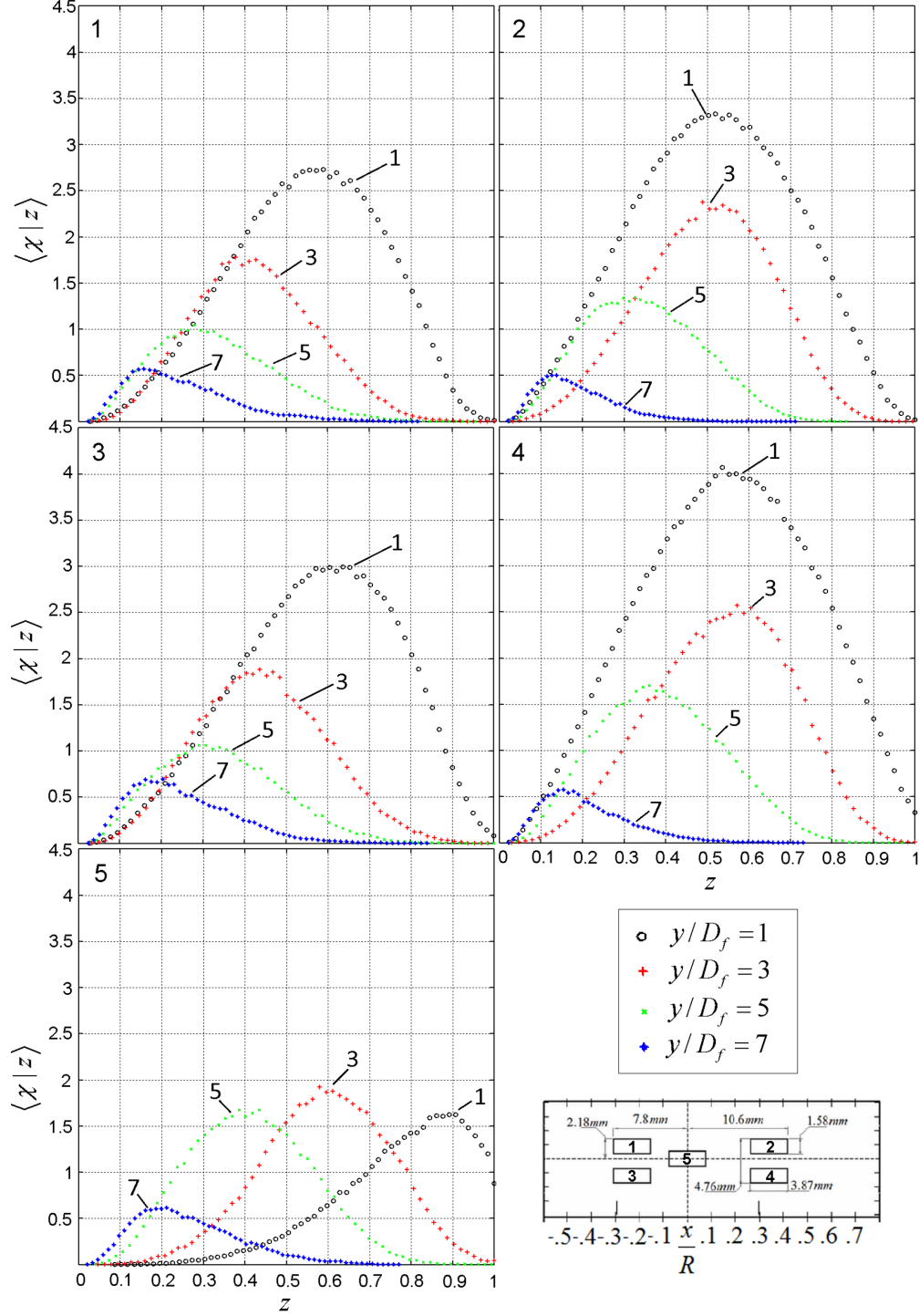
FIG. 29. Mean scalar dissipation rate conditional on mixture fraction, as a function of axial distances and window locations for S=0.3. Window dimensions are 1.58 mm × 3.87 mm ($\approx 4\lambda_\beta \times 10\lambda_\beta$) and their locations are shown in bottom right corner and in Figure 3.
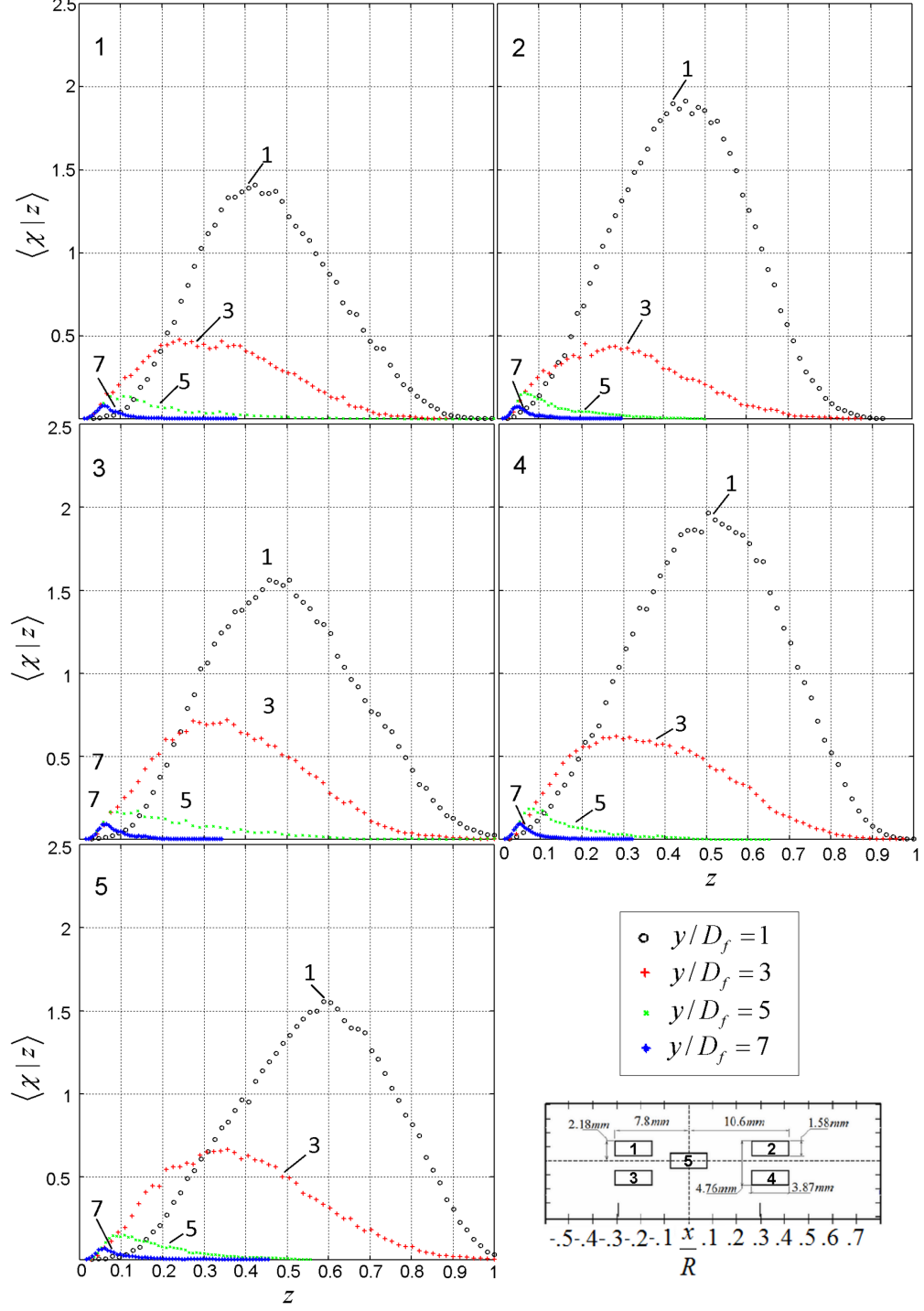
46

FIG. 30. Mean scalar dissipation rate conditional on mixture fraction, as a function of axial distances and window locations for S=0.58. Window dimensions are 1.58 mm × 3.87 mm ($\approx 4\lambda_\beta \times 10\lambda_\beta$) and their locations are shown in bottom right corner and in Figure 3.

FIG. 31. Mean scalar dissipation rate conditional on mixture fraction, as a function of axial distances and window locations for S=1.07. Window dimensions are 1.58 mm × 3.87 mm ($\approx 4\lambda_\beta \times 10\lambda_\beta$) and their locations are shown in bottom right corner and in Figure 3.
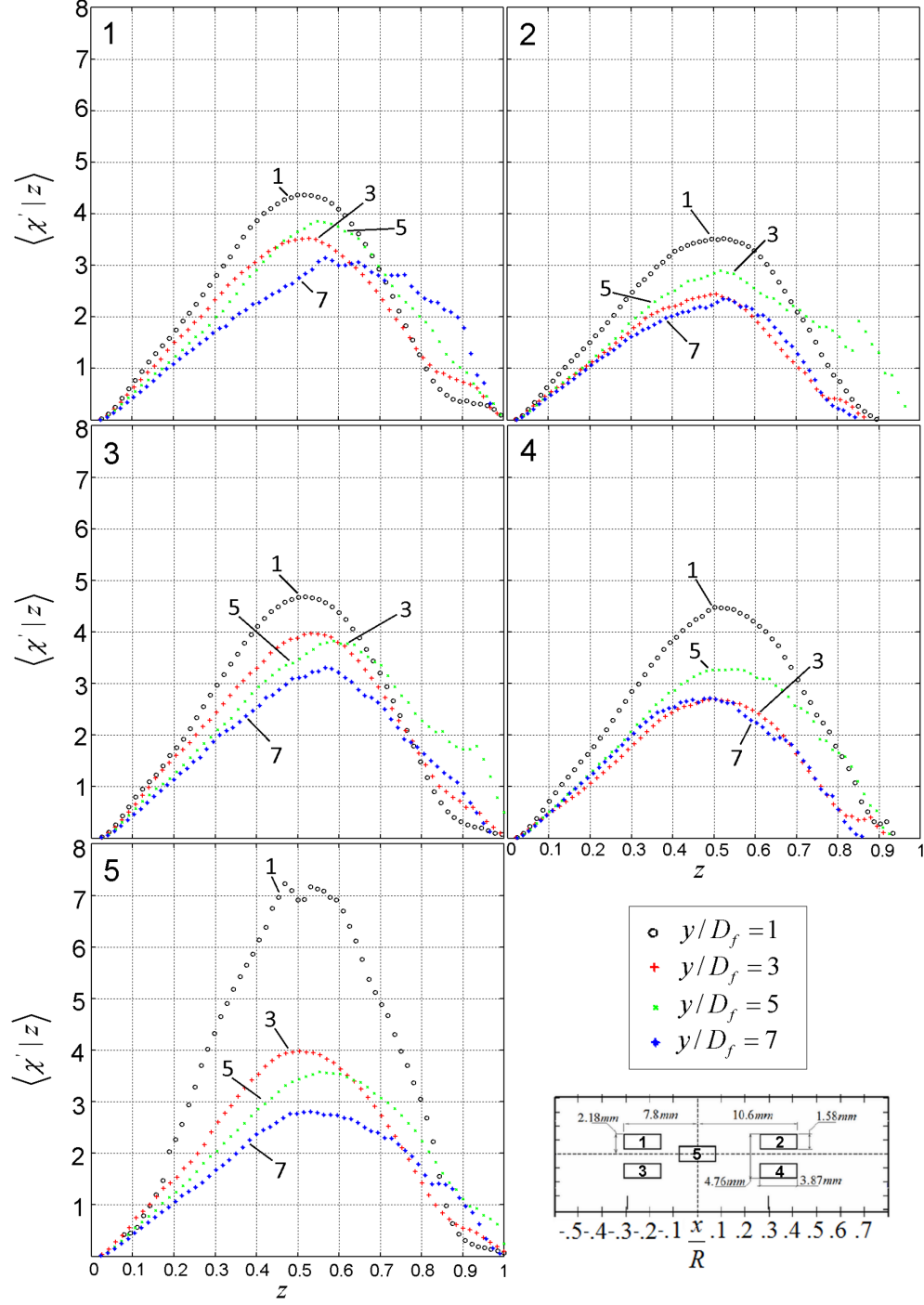
48

FIG. 32. Standard deviation of scalar dissipation rate conditional on mixture fraction, as a function of axial distances and window locations for S=0.3. Window dimensions are 1.58 mm × 3.87 mm ($\approx 4\lambda_\beta \times 10\lambda_\beta$) and their locations are shown in bottom right corner and in Figure 3.
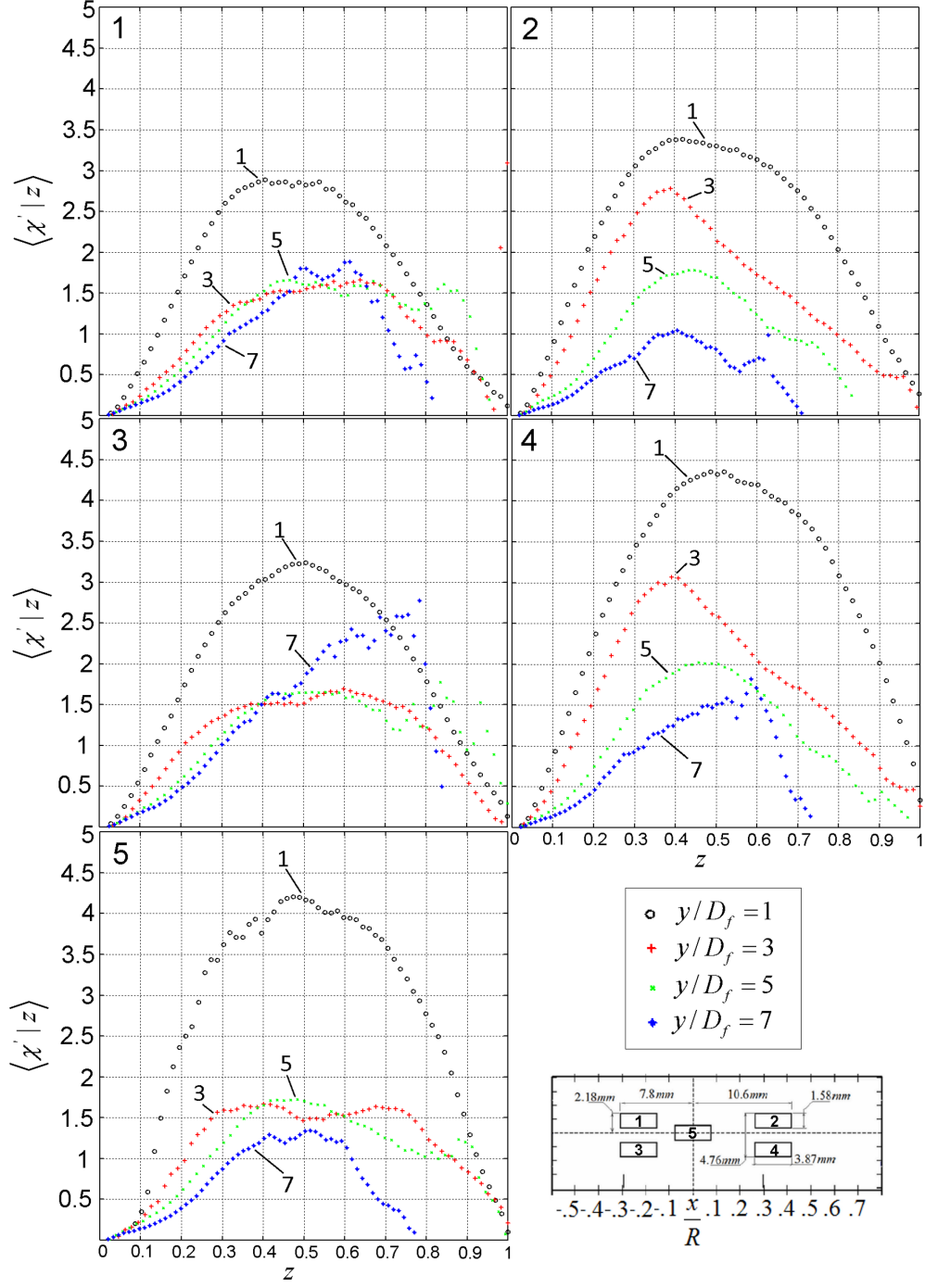
49

FIG. 33. Standard deviation of scalar dissipation rate conditional on mixture fraction, as a function of axial distances and window locations for S=0.58. Window dimensions are 1.58 mm × 3.87 mm ($\approx 4\lambda_\beta \times 10\lambda_\beta$) and their locations are shown in bottom right corner and in Figure 3.
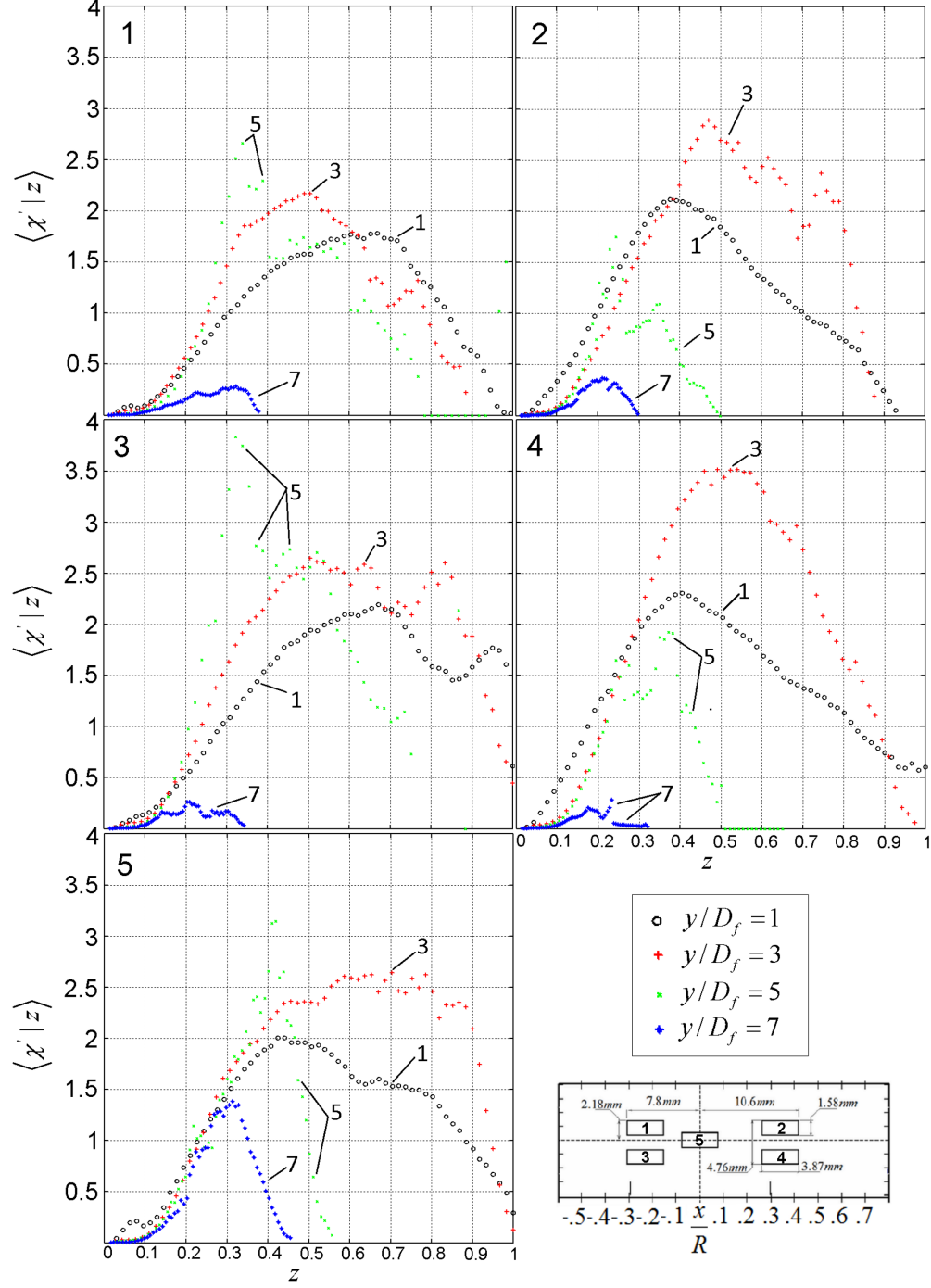
50

FIG. 34. Standard deviation of scalar dissipation rate conditional on mixture fraction, as a function of axial distances and window locations for S=1.07. Window dimensions are 1.58 mm × 3.87 mm ($\approx 4\lambda_\beta \times 10\lambda_\beta$) and their locations are shown in bottom right corner and in Figure 3.
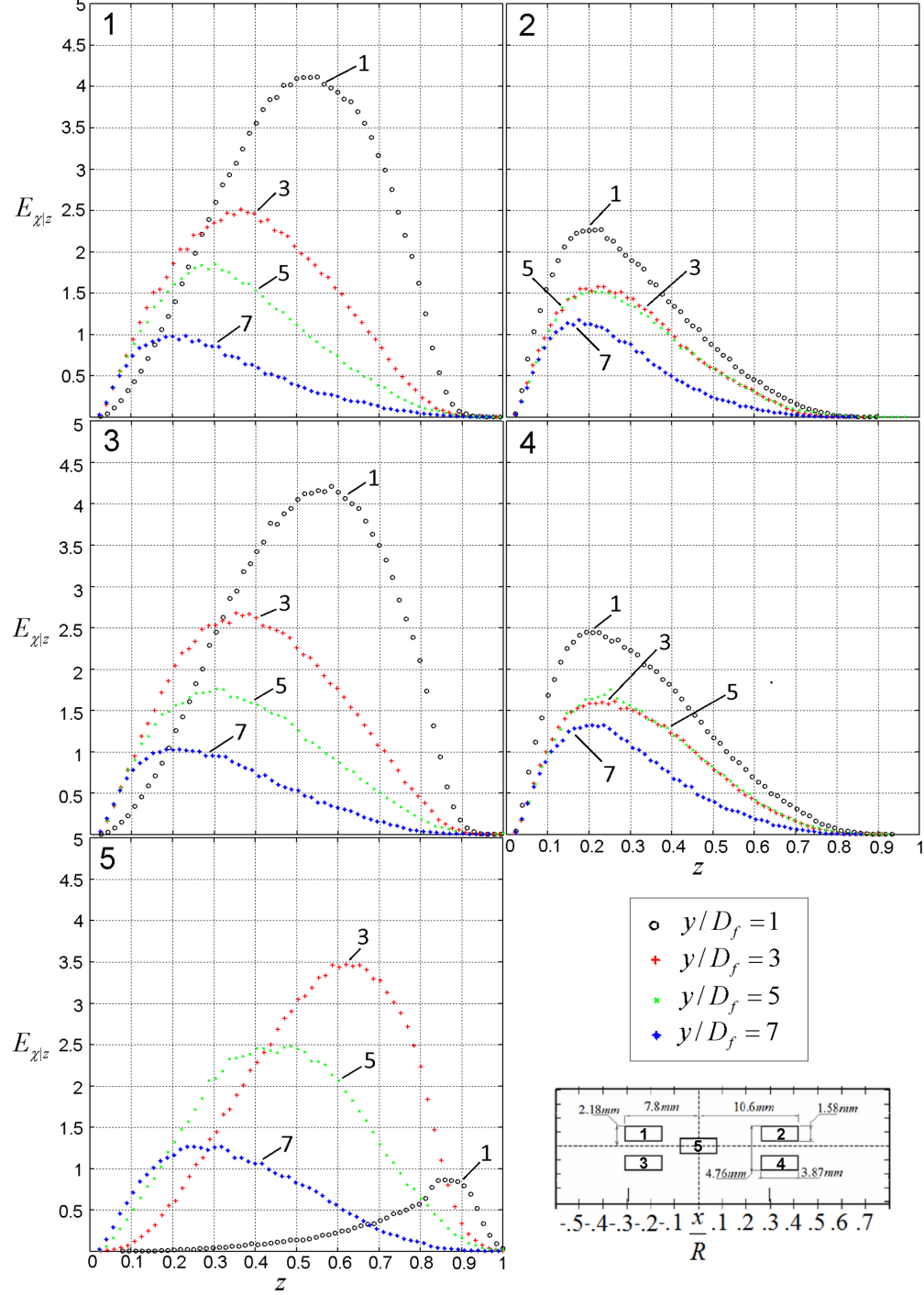
FIG. 35. Weighted probability of occurrence of the mean conditional scalar dissipation rate for S=0.3 as a function of axial distances and window locations for S=0.3. Window dimensions are 1.58 mm × 3.87 mm ($\approx 4\lambda_\beta \times 10\lambda_\beta$) and their locations are shown in bottom right corner and in Figure 3. Note that the weighted probability of occurrence of the mean conditional scalar dissipation coincides with the conditional mean of the scalar dissipation rate (similar for S=0.58 and 1.07).

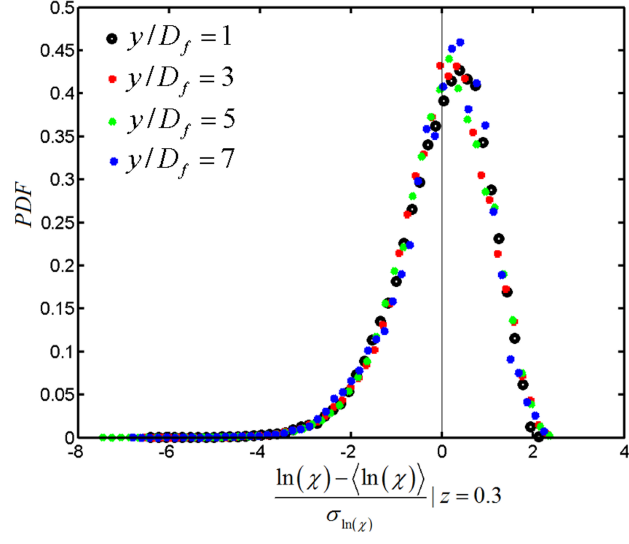FIG. 36. Conditional probability for S=0.58 at $y/D_f = 1 - 7$ computed for window 2 (Figure 3). Conditional probability is shown for z=0.3. Conditional probabilities for other z demonstrate similar trend and are not shown here.

IV. CONCLUSIONS

The scalar dissipation rate was measured in a turbulent isothermal swirling non-reacting flow, where a central axial jet was injected in a swirling annular flow. The flow has typical geometry of swirl-stabilised burners. The swirling annular flow Reynolds number was 29000 based on area-averaged velocity of 8.46 m/s and a diameter of 50.8 mm. The scalar dissipation rate was computed from two-dimensional measurements of the mixture fraction based, on laser induced acetone fluorescence using the associated spatial gradients of mixture fraction as a function of axial distance (along the flow centreline) and radial locations (perpendicular to main flow direction) up to 2 outer (annular) nozzle diameters from the burner. The swirl number was varied and the values of 0.3, 0.58, 1.07 were measured. A procedure, based on Wiener-Kolmogorov filtering theory, was used to denoise the raw mixture fraction images obtained from the planar laser induced fluorescence of acetone. The scalar dissipation rate filtering errors were up to 15%, depending on downstream positions from the burner exit and swirl number.

The general observation was that the scalar dissipation rate increased with the increase of swirl number for axial positions $y/D_f = 1, 3, 5$. The maximum value of instantaneous scalar dissipation rate was found to be up to 35 s^{-1}. The values of the mean scalar dissipation rate were around 6 times smaller than the instantaneous values. The higher mean scalar dissipation rate occurred at the near nozzle regions and at the fuel jet periphery, where the mixture fraction gradients were the largest. The probability density functions of the logarithm of the scalar dissipation rate fluctuations were found to be slightly negatively skewed at low swirl number (S=0.3) and almost symmetrical when the swirl number increased to 0.58 and 1.07.

The joint probability density functions of the scalar fluctuations and the scalar dissipation rate were computed and compared with the product of the individual p.d.fs. in order to evaluate the statistical independence between the scalar and its dissipation rate. Five spatial locations were chosen to represent both homogeneous and highly segregated scalar fields, i.e shear layer and centreline. Window dimensions were chosen on the basis of sufficient number of samples. At all five locations in the flow, the contours, of the product of the individual p.d.fs. followed a circular pattern, even though not entirely symmetric. The contours of the joint p.d.f. had a little oval shape and seemed skewed towards both negative and

54

positive dissipation rate fluctuations. The statistical independence (between scalar and its dissipation rate) was therefore in better agreement with the experimental data for regions of homogeneous scalar field or well-mixed regime, which corresponded to higher axial locations and large swirl number.

The mean of the scalar dissipation rate conditioned on the mixture fraction, standard deviation of the scalar dissipation rate, the weighted probability of occurrence of the mean conditional scalar dissipation rate and the conditional probability were also reported. The conditional mean scalar dissipation rate increased with the mixture fraction reaching a maximum value for different mixture fraction values (depending on y/D_f and S). For low swirl numbers, the conditional mean had distinct parabolic shape, while for high swirl numbers and high y/D_f, the shape could not be characterised by a simple distribution, e.g. parabolic, Gaussian etc. The standard deviation of fluctuations of scalar dissipation rate conditioned on mixture fraction demonstrated similar trend as the conditional mean with similar bell-shaped curve. The weighted probability of occurrence of the mean conditional scalar dissipation rate was bell-shaped and positively skewed and followed the conditional mean pattern. The maximum values of the weighted probability were similar to those in the conditional mean for all swirl numbers.

ACKNOWLEDGMENTS

REFERENCES

[1]N. Peters, "Local turbulent quenching due to flame stretch and non-premixed turbulent combustion," Combust. Sci. Tech. **30** (1983).

[2]R. W. Bilger, "The structure of turbulent nonpremixed flames," In 22th Symposium (Intl.) on Combustion **22**, 475 (988).

[3]Y. Y. Lee and S. B. Pope, "Nonpremixed turbulent reacting flow near extinction," Combustion and Flame **101**, 501 (1995).

[4]S. K. Liew, K. N. C. Bray and J. B. Moss, "A stretched laminar flamelet model of turbulent non-premixed combustion," Combustion and Flame **56**, 199 (1984).

[5]J. Janicka and N. Peters, "Prediction of turbulent jet diffusion flame lift-off using a pdf transport equation," 19th Symposium (Intl.) on Combustion, The Combustion Institute, Pittsburgh, 367 (1982).

[6]A. N. Kolmogorov, "A refinement of previous hypothesis concerning the local structure of turbulence in a viscous incompressible fluid at high Reynolds number," J. Fluid Mech. **13**, 82 (1962).

[7]G. Blanquart and H. Pitsch, "Modeling autoignition in non-premixed turbulent combustion using a stochastic flamelet approach," Proc. Combust. Inst. **30**, 2745 (2005).

[8]O. Soulard, V. Sabelnikov and M. Gorokhovski, "Stochastic scalar mixing models accounting for turbulent frequency multiscale fluctuations," Int. J. Heat Fluid Flow **25**, 875 (2004).

[9]H. Pitsch and S. Fedotov, "Investigation of scalar dissipation rate fluctuations in non-premixed turbulent combustion using a stochastic approach," Combust. Theor. Model. **5**, 41 (2000).

[10]M. Oberlack, R. Arlitt and N. Peters, "On stochastic Damkohler number variations in a homogeneous flow reactor," Combust. Theor. Model. **4**, 495 (2000).

[11]A. Klimenko and R. W. Bilger, "Conditional moment closure for turbulent combustion," Prog. Energy Combust. Sci. **25**, 595 (1999).

[12]A. Sahay, E. O'Brien, "Uniform mean scalar gradient in grid turbulence: conditioned dissipation and production," Phys. Fluids A **5**, 1076 (1993).

[13]R. W. Bilger, "The structure of diffusion flames," Combustion Science and Technology, **13**,155 (1976a).

[14]E. Mastorakos, T. A. Baritaud, and T. J. Poinsot, "Numerical simulations of autoignition in turbulent mixing flows,"Combustion and Flame **109**, 198 (1997).

[15]G-H. Wang, N. T. Clemens, R. S. Barlow and P. L. Varghese," A system model for assessing scalar dissipation measurement accuracy in turbulent flows", Meas. Sci. Technol., **18**, 5 (2007).

[16]G. H. Wang and N. T. Clemens, "Effects of imaging system blur on measurements of flow scalars and scalar gradients," Exp. in Fluids **37**, 194 (2004).

[17]R. W. Dibble, W. Kollman and R. W. Schafer, "Measurements and predictions of scalar dissipation in turbulent jet flames," 20th Symposium (Int.) on Combustion/The Combustion Institute, 345 (1984).

[18]E. Effelsberg and N. Peters, "Scalar dissipation rates in turbulent jets and jet diffusion flames," 22nd Symposium (Intl.) on Combustion/The Combustion Institute, 693 (1988).

[19]K. Sardi, A. M. K. P. Taylor and J. Whitelaw, "Conditional scalar dissipation statistics in a turbulent counterflow," J. Fluid Mech. **361**, 1 (1998).

[20]J. A. Sutton and J. F. Driscoll, "Scalar dissipation rate measurements in flames. A method to improve spatial resolution by using nitric oxide PLIF," Proceedings of the Combustion Institute **29**, 2727 (2002).

[21]D.C. Kyritsis, V.S. Santoro and A. Gomez, "Quantitative scalar dissipation rate measurements in vortex-perturbed counterflow diffusion flames," Proceedings of the combustion institute **29**, 1679 (2002).

[22]D. Wang and C. Tong, "Experimental study of velocity-scalar filtered joint density function for LES of turbulent combustion," Proc. of the Combustion Institute **30**, 567 (2005).

[23]C. N. Markides and E. Mastorakos, "Measurements of scalar dissipation in a turbulent plume with planar laser-induced fluorescence of acetone," Chemical Engineering Science **61**, 2835 (2006).

[24]N. Soulopoulos, *Experimental investigation of scalar mixing in unsteady turbulent jets,* PhD thesis Imperial College London, Mechanical Engineering Department, April 2009.

[25]S. F. Ahmed, "Scalar dissipation rate statistics in turbulent flows using planar laser Induced fluorescence measurements," Int. Journal of Heat and Fluid Flow **33**, 220 (2012). http://www.sciencedirect.com/science/article/pii/S0142727X11001627

[26]Jayesh and Z. Warhaft, "Probability distribution, conditional dissipation and transport of

passive temperature fluctuations in grid generated turbulence," Phys. Fluids A **4**, 1992.

[27]P. Kailasnath, K.R. Sreenivasan and J.R. Saylor, "Conditional scalar dissipation rates in turbulent wakes, jets and boundary layers," Phys. Fluids A **5**, 1993

[28]F. Anselmet and R.A. Antonia, "Joint statistics between temperature and its dissipation," Phys. Fluids **28**, 1985.

[29]T. F. Dixon, J. S. Truelove and T. F. Wall, "Aerodynamic studies on swirled coaxial jets from nozzles with divergent quarls," J. of Fluids Eng. **105**, 197 (1983).

[30]V. D. Milosavljevic, *Natural gas, kerosene and pulverized fuel fired swirl burners,* PhD thesis (Imperial College of Science Technology and Medicine. Department of Mechanical Engineering. July 1993).

[31]W. Steenbergen, *Turbulent pipe flow with swirl,* PhD thesis (Technishe Universiteit Eindhoven, Netherlands, 1995).

[32]N. Soulopoulos, Y. Hardalupas, and A. M. K. P. Taylor, "Scalar dissipation rate measurements in a starting jet," Exp. in Fluids **55**, 1 (2014).

[33]M. Petrou, and P. Bosdogianni, *Image processing: the fundamentals* (John Wiley & Sons Ltd. 1999).

[34]F. J. Krawczynski, B. Renou, L. Danaila, and F. X. Demoulin, "Small-scale measurements in a partially stirred reactor," Exp. in fluids **40**, 667 (2002).

[35]M. C. Thurber, "Acetone laser-induced fluorescence for temperature and multiparameter imaging in gaseous flows," Topical Report TSD-120, Thermosciences Division, Department of Mechanical Engineering, Stanford University, Stanford, California 94305-3032 U.S.A, March 1999.

[36]D. A. Everest, J. F. Driscoll, W. J. A. Dahm, and D. A. Feikema, "Images of two dimensional field and temperature gradients to quantify mixing rates within a nonpremixed turbulent jet flame," Combustion and Flame **101**, 58 (1995).

[37]M. Namazian, R. W Scheffer and J. Kelly, "Scalar dissipation measurements in the developing region of a jet," Combustion and Flame **74**, 147 (1988).

[38]K. R. Sreenivasan , R. A. Antonia and H. Q. Dahn, "Temperature dissipation fluctuaids in a turbulent boundary layer," Phys. of Fluids **20**, 1238 (1977).

[39]W. J. A. Dahm and K. A. Buch, "Lognormality of the scalar dissipation PDF in turbulent flows," Phys. of Fluids **1**, 1290 (1989).

[40]H. Tennekes and J. L. Lumley, *A first course in turbulence* (The MIT press 1972).

[41]V. Stetsyuk, N. Soulopoulos, Y. Hardalupas, and A. M. K. P. Taylor, "Experimental assessment of presumed filtered density function models," Phys. Fluids **27**, 065107 (2015), doi: 10.1063/1.4922169.

[42]V. Stetsyuk, *Experimental study of combustion and scalar mixing in swirling jet flows,* PhD thesis (Imperial College London, Department of Mechanical Engineering. February 2014).